AUSTEMPERED DUCTILE IRONS WITH SUPERIOR MECHANICAL PROPERTIES DESIGNED BY UTILIZING A COMPUTATIONAL DESIGN APPROACH

A THESIS SUBMITTED TO
THE GRADUATE SCHOOL OF NATURAL AND APPLIED SCIENCES
OF
MIDDLE EAST TECHNICAL UNIVERSITY

BY

CANER YALÇINER

IN PARTIAL FULFILLMENT OF THE REQUIREMENTS
FOR
THE DEGREE OF MASTER OF SCIENCE
IN
METALLURGICAL AND MATERIALS ENGINEERING

SEPTEMBER 2023

Approval of the thesis:

AUSTEMPERED DUCTILE IRONS WITH SUPERIOR MECHANICAL PROPERTIES DESIGNED BY UTILIZING A COMPUTATIONAL DESIGN APPROACH

submitted by **CANER YALÇINER** in partial fulfillment of the requirements for the degree of **Master of Science** i**n Metallurgical and Materials Engineering, Middle East Technical University** by,

Prof. Dr. Halil Kalıpçılar
Dean, Graduate School of **Natural and Applied Sciences** _____

Prof. Dr. Ali Kalkanlı
Head of the Department, **Metallurgical and Materials Eng.** _____

Assoc. Prof. Dr. Caner Şimşir
Supervisor, **Metallurgical and Materials Eng., METU** _____

Examining Committee Members:

Prof. Dr. Cemil Hakan Gür
Metallurgical and Materials Eng, METU _____

Assoc. Prof. Dr. Caner Şimşir
Metallurgical and Materials Eng, METU _____

Assist. Prof. Dr. Irmak Sargın
Metallurgical and Materials Eng, METU _____

Prof. Dr. Yunus Eren Kalay
Metallurgical and Materials Eng, METU _____

Assoc. Prof. Dr. Volkan Kılıçlı
Metallurgical and Materials Eng, Gazi University _____

Date: 07.09.2023

I hereby declare that all information in this document has been obtained and presented in accordance with academic rules and ethical conduct. I also declare that, as required by these rules and conduct, I have fully cited and referenced all material and results that are not original to this work.

Name Last name : Caner Yalçıner

Signature :

ABSTRACT

AUSTEMPERED DUCTILE IRONS WITH SUPERIOR MECHANICAL PROPERTIES DESIGNED BY UTILIZING A COMPUTATIONAL DESIGN APPROACH

Yalçıner, Caner
Master of Science, Metallurgical and Materials Engineering
Supervisor : Assoc. Prof. Dr. Caner Şimşir

September 2023, 87 pages

Given its unique microstructure providing the opportunity to have high strength, ductility, and toughness, austempered ductile iron (ADI) finds applications in various industries, including automotive, agriculture, energy, defense. This typical microstructure consists of acicular bainitic ferrite, graphite nodules, and retained austenite phases. Fine acicular ferrite formed during austempering treatment provides high strength and hardness to the material. Nevertheless, it is essential to note that the size of this ferrite phase plays a significant role in this context. Graphite nodules bring in ductility and arrest the cracks within the structure, thereby preventing their propagation. However, achieving a high nodularity percentage and ensuring the homogeneous distribution is imperative. Moreover, retained austenite in the microstructure undergoes stress-induced transformation when subjected to applied stress, enhancing material's wear resistance. However, this behavior depends on the stability level of the retained austenite phase. This stability level is determined by chemical composition and morphology of retained austenite phase.

Taking all these effects into consideration, it is believed that it is possible to develop new Austempered Ductile Iron (ADI) materials with superior mechanical properties

compared to conventional ones, provided that the necessary adjustments are made to the microstructure. This study aims to design two distinct ADIs: one with ultra-high strength and moderate toughness, and another with high strength and high toughness. The design processes involve modifications in chemical compositions and heat treatment scenarios, utilizing the CALPHAD (CALculation of PHAse Diagrams) approach. These production parameters are specified to yield samples with varying microstructures, including different volume fractions of retained austenite with distinct chemical compositions, and varying sizes of ausferrite phases. Simultaneously, the goal is also to achieve a high level of nodularity and ensure a uniform distribution of the graphite phase. The mechanical properties of these samples are assessed through Brinell hardness tests, tensile tests, and impact tests at room temperature.

In conclusion, aside from achieving the study objective, this thesis demonstrates the utility and consistency of the computational design methodology employed within its scope.

Keywords: Austempered Ductile Iron, Austempering Treatment, CALPHAD Approach, Integrated Heat Treatment and Alloy Design, Computational Materials Design

ÖZ

HESAPLAMALI TASARIM YAKLAŞIMI KULLANILARAK TASARLANMIŞ ÜSTÜN MEKANİK ÖZELLİKLERE SAHİP ÖSTEMPERLENMİŞ KÜRESEL GRAFİTLİ DÖKME DEMİRLER

Yalçıner, Caner
Yüksek Lisans, Metalurji ve Malzeme Mühendisliği
Tez Yöneticisi: Doç. Dr. Caner Şimşir

Eylül 2023, 87 sayfa

Östemperlenmiş küresel grafitli dökme demir, yüksek mukavemet, süneklik ve tokluk gibi üstün mekanik özelliklere sahip olan ve bu özellikleri sayesinde de otomotiv, tarım, enerji, savunma vb. birçok endüstride kullanılan bir malzemedir. Bu özellikleri, iğnemsi beynitik ferrit, grafit nodülleri ve kalıntı östenit fazlarından oluşan benzersiz mikroyapısından kaynaklanmaktadır. Östemperleme işlemi sırasında oluşan ince iğnemsi ferrit, malzemeye yüksek mukavemet ve sertlik sağlar. Belirtmek gerekir ki, iğnemsi ferritin boyutu bu bağlamda önemli bir rol oynamaktadır. Grafit nodülleri, süneklik sağlar ve yapı içerisinde bulunan çatlakları durdurarak ilerlemesini önleyici bir davranış sergiler. Bu davranışın etkili olabilmesi için yüksek nodülerite yüzdesine ulaşmak ve homojen dağılımı sağlamak esastır. Mikroyapıdaki kalıntı östenit, uygulanan stres altında stresle indüklenen dönüşüme uğrar ve mikroyapının aşınma direncini arttırır. Bu davranış, kalıntı östenit fazının stabilite düzeyine bağlıdır. Bu stabilite seviyesi, kalıntı östenit fazının kimyasal bileşimi ve morfolojisi ile belirlenir.

Bütün bu etkiler göz önünde bulundurularak, mikroyapıda gerekli ayarlamalar yapılırsa, geleneksel olanlardan daha üstün mekanik özelliklere sahip yeni

östemperlenmiş küresel grafitli dökme demirler geliştirilebileceğine inanılmaktadır. Bu çalışma, biri çok yüksek mukavemet ve orta seviye toklukta, diğeri yüksek mukavemet ve yüksek toklukta olmak üzere iki farklı östemperlenmiş küresel grafitli dökme demir tasarlamayı amaçlamaktadır. Tasarım süreçleri, CALPHAD (Faz Diyagramlarının Hesaplanması) yaklaşımı kullanılarak, üretilecek olan numuneler için farklı kimyasal bileşimler ve ısıl işlem senaryoları belirlenerek gerçekleştirilmiştir. Bu üretim parametreleri, farklı kimyasal bileşimlere sahip farklı kalıntı östenit hacim fraksiyonları ve farklı ösferrit faz boyutları dahil olmak üzere değişken mikroyapılara sahip numuneler elde etmek amacıyla belirlenmiştir. Aynı zamanda, grafit fazı için yüksek nodülarite ve homojen bir dağılım elde edilmesi hedeflenmiştir. Bu numunelerin mekanik özellikleri, oda sıcaklığında Brinell sertlik testleri, çekme testleri ve darbe testleri ile değerlendirilmiştir.

Sonuç olarak, bu tez, belirlenen tasarım hedeflerine ulaşmanın yanı sıra, kapsamı dahilinde kullanılan hesaplamalı tasarım metodolojisinin faydalarını ve tutarlılığını göstermektedir.

Anahtar Kelimeler: Östemperlenmiş Küresel Grafitli Dökme Demir, Östemperleme Isıl İşlemi, CALPHAD Metodolojisi, Bütünleşik Isıl İşlem ve Alaşım Tasarımı, Hesaplamalı Malzeme Tasarımı

To my wife, family, and friends.

ACKNOWLEDGMENTS

I would like to express my deepest gratitude to my supervisor Assoc. Prof. Caner Şimşir for his invaluable guidance, mentorship, and unwavering support throughout my thesis journey. His expertise, dedication, and encouragement have been instrumental in shaping the direction and quality of my research. I am truly grateful for his mentorship, patience, and constant motivation.

I would like to extend my sincere appreciation to FNSS Savunma Sistemleri A.Ş., Döksan Isıl İşlem A.Ş., and Simultra Malzeme Teknolojileri for their support in providing resources, facilities, and access to the data that have been crucial to the successful completion of my thesis. The collaborative environment and opportunities offered by these organizations have greatly enriched my research experience.

I would like to acknowledge Mr. Barış Çetin for his technical assistance and insightful input. His expertise and guidance have been invaluable in enhancing the technical aspects of my thesis.

I would like to thank my managers in FNSS Savunma Sistemleri A.Ş., Mr. Arda Güleş and Mr. Hakan Yağcı, for their consistent support throughout my master's program.

I wish to thank my fellow travelers throughout my academic journey, Andaç Özsoy, Oğuzhan Bulut, Yiğit Kemal Ökten and Yusuf Alptuğ Polat, for their valuable perspective, encouragement, support, and most importantly, friendship.

I would like to express my heartfelt gratitude to my beloved parents and brother for always being by my side and supporting me whenever I needed. Their belief in me has been a constant source of motivation.

Last but not least, I am profoundly grateful to my wife, Merve Yalçıner, whose endless support and boundless encouragement have been a constant source of strength in every aspect of my life. I am truly fortunate to have her by my side.

TABLE OF CONTENTS

LIST OF TABLES

TABLES

LIST OF FIGURES

FIGURES

CHAPTER 1

INTRODUCTION AND LITERATURE REVIEW

1.1 Austempered Ductile Iron

According to ASTM A644, austempered ductile iron (ADI) is a ductile cast iron whose microstructure consists of acicular ferrite and high carbon retained austenite phases, called ausferrite. This type of cast iron is produced by conducting a controlled special thermal process, known as austempering.[1] Ductile iron was discovered in 1943 through the development of magnesium as a graphite spherodizer by Keith Millis. It was patented in 1949, while the austempering process had been around a decade earlier. Although it was not commercialized until 1972[2], the combination of these provides an opportunity to have excellent mechanical properties together. Thanks to its unique microstructure, ADI can exhibit high strength, ductility, toughness, good damping capability, and excellent wear and fatigue resistance.[3,4] The fine acicular ferrite structure provides high strength and hardness. Simultaneously, the presence of retained austenite and graphite nodules renders iron ductile. Furthermore, the high carbon retained austenite phase undergoes stress-induced transformation when exposed to applied stress, making the structure remarkably wear resistant. Additionally, graphite nodules act as crack arrestors and preventing the crack propagation within the structure, thus enhancing both fatigue life and damping capability.[5–8] In addition to these benefits, it is an eco-friendly material since it is 100% recyclable.[7] ADI provides an opportunity to obtain a wide range of mechanical properties through the customization of production parameters, including the heat treatment parameters and the type and quantity of alloying elements. In ASTM A897 Standard, it is graded from 1 to 5 based on its mechanical properties, the corresponding minimum requirements for these properties are shared in Table 1[9].

Table 1. Minimum Mechanical Property Requirements with Respect to ADI Levels

Mechanical Properties	***Levels***				
	I	***II***	***III***	***IV***	***V***
Tensile Strength (MPa)	850	1050	1200	1400	1600
Yield Strength (MPa)	550	700	850	1100	1300
Elongation (%)	11	10	7	5	3
Hardness (HB)	269-321	302-363	341-444	388-477	444-555
Impact Energy (J)	100	80	60	35	N/A

When ADI is compared to its equivalent aluminum and steel materials, it provides a weight and cost advantage at a given yield strength. Besides, it exhibits twice the strength for a given level of ductility with respect to the ferritic and martensitic structures obtained through common heat treatment techniques. Unsurprisingly, the combination of these advantageous characteristics and good mechanical properties makes ADI an attractive material to be used in many industries such as automotive, agriculture, energy, defense, etc. For example, since it has good fatigue resistance and damping capability, some of the suspension parts have started to be produced from ADI in the past century. Besides suspension parts, crankshafts, transmissions, and various gears can also be produced from ADI. Another example, since it has excellent wear resistance, some gears in the automotive industry and the parts like ploughshares and dozer blades, which are subjected to friction during their intended usage, can be produced from ADI.[7,8,10–16] Moreover, recently, it is also believed that it can be a potential material to be used in ballistic applications. The armor materials are expected to be hard enough to be able to blunt the projectile tip and tough enough to absorb the shock resulting from the impact. Moreover, they are also expected to have good wear resistance against the incoming projectiles.[17–19] Since ADI shows high strength, toughness, and good wear resistance at the same time, studies are being conducted to determine its potential usage in that field. [20–22]

In a nutshell, ADI is a specialized heat-treated nodular cast iron that exhibits an exceptional combination of mechanical properties while maintaining the cost and weight-saving potential. Given all the advantages it offers, it is seen as a candidate material for many different applications in several industries. However, achieving the desired properties requires meticulous control of every parameter in the production process. These parameters and their effects are explained in detail in the following sections.

1.1.1 Parameters Affecting Mechanical Properties

As mentioned in the previous section, ADI exhibits outstanding mechanical properties owing to its unique microstructure, comprising carbon-free acicular ferrite, retained austenite, and graphite nodules. Achieving this microstructure necessitates precise adjustment of production parameters, including chemical composition, austenitization temperature and time, cooling rates, austempering temperature and time and quenching temperature. For instance, graphite nodules primarily contribute to ADI's ductility by blunting crack propagation within the microstructure, thereby providing excellent fatigue life and damping capability. It's important to note that the nodularity, size, and distribution of graphite nodules are critical factors in this regard. Uniform distribution is essential for the material to exhibit homogeneous properties throughout, as it directly affects diffusion kinetics during the heat treatment processes.[23–25] Moreover, adjustments in the chemical composition, austenitization temperature, and the rate of the following cooling process are necessary to prevent the formation of undesired phases, such as pearlite, to be able to obtain desired mechanical properties.[26] As it is remarked by these examples, all the process parameters must be carefully determined by considering their implications, which are detailed in this section.

1.1.1.1 Chemical Composition

Si, Mn, Cu, Ni, and Mo are the commonly used alloying elements in ADI casting. Each of these alloying elements individually has different effects on transformation kinetics, hence the final microstructure and final properties.[27,28] For this reason, their contents should be tailored in line with the expectations of the final product.

Three critical factors need to be taken into consideration when tailoring the chemical composition of austempered ductile iron. First of all, iron should be sufficiently alloyed to prevent the pearlite formation during which the cooling operation from austenitization temperature to austempering temperature. However, if it is over-alloyed, austempering reactions might be delayed. Secondly, the final microstructure should be free of intergranular carbides or phosphates. Finally, the constituents must be uniformly distributed throughout the casting to eliminate chemical segregations as much as possible.[29] By considering these, the type and content of the alloying elements must be determined with caution. The commonly used elements in ADI and their effects are shared in detail below.

Carbon: In a typical austempered ductile iron, the weight percentage of carbon is between 3.4 and 3.8. An increase in the carbon content increases the tensile strength of the iron, however after some point, graphite flotation, which deteriorates the mechanical properties, may take place. More precisely, it depends on the carbon equivalent (CE) but the upper limit of CE in terms of the formation of graphite flotation is determined by the section thickness.[6,30,31]

Silicon: Silicon is one of the important elements in austempering ductile iron since it promotes the graphite formation during austenitization and suppresses the formation of carbides during austempering operation, resulting in better mechanical properties. Besides, it forms a silicon-rich surface layer protecting the iron against oxidation and improving its performance at elevated temperatures. The weight percentage of silicon is generally between 2.4 – 2.8.[27,32–35]

Molybdenum: Molybdenum is the most effective element in terms of increasing hardenability and austemperability. It also enhances the performance that the

material exhibits at elevated temperatures. It increases ductility and tensile strength, however, after a certain weight percentage value (~0.3 wt.%), it causes a slight decrease in both by segregating as carbides at intercellular locations during solidification.[27,28,32,34,36]

Manganese: Manganese is an austenite stabilizer element, and it is used to enhance hardenability and austemperability, however, it forms carbides at grain boundaries during solidification, slowing the austempering reactions. In other words, it restricts and can even close the processing window, thus preventing the completion of ausferrite formation and it may result in martensite formation due to the presence of low-carbon austenite. Besides, it causes shrinkage and negatively affects machinability. For these reasons, the weight percentage of the manganese is suggested to be kept lower than 0.3 wt.%.[27,28,32,34]

Copper: Like manganese, copper increases the hardenability of iron. It increases tensile strength and hardness without causing embrittlement in the matrix. However, it is a pearlite stabilizer element and after 0.8 wt.%, it may create diffusion barriers around the graphite nodules and restricts the carbon diffusion during the austenitization process.[24,27,32,34] It has also a positive effect on austemperability.[37,38]

Nickel: Nickel is an austenite stabilizer element and in ADI, it is used to improve hardenability and austemperability. It enhances fracture toughness and ductility properties, whereas it slightly decreases tensile strength. However, if it is used more than 2 wt.%, aside from cost issues, it may cause an increase in the volume of retained austenite that does not undergo austempering reactions, resulting in some embrittlement problems.[27,28,32,34,36]

Although manganese, copper, nickel, and molybdenum all are added for an increase in hardenability and austemperability, the reason that the allowed weight percentages of copper and nickel are higher than those of manganese and molybdenum is that copper and nickel do not segregate as much as molybdenum and manganese do, instead they partition into the solid phase.[29,39] Segregation of substitutional elements gives rise to carbon segregation in the grain boundary regions after the

austenitization process, thus inhomogeneity in austempering kinetics and a decrease in processing window takes place.[39] Nevertheless, these elements are used together rather than adding only copper and nickel since they exhibit considerably greater effects when they are used together.[12,29,40]

In addition to aforementioned elements, other elements such as Al, Cr, B, Co, and micro-alloying elements like Ti, V and Nb can also be given a place in austempered ductile iron castings.[27]

1.1.1.2 Heat Treatment

Just as chemical composition, adjustment of heat treatment process parameters is of great importance to acquire convenient microstructure bringing in desired mechanical properties. In this context, ADI has a special heat treatment process starting with an austenitization process taken place typically at between 850 – 950 °C for sufficient times to obtain a matrix consisting of a full austenite phase saturated with carbon. After austenitization, iron is cooled down to a temperature (typically at between 250 – 450 °C) at which the isothermal treatment called austempering is taken place.[26,29,41,42] During austempering treatment, two different transformation reactions take place one after another:

Stage I: $\gamma \rightarrow \alpha + \gamma_{hc}$

Stage II: $\gamma_{hc} \rightarrow \alpha$ + Carbide

γ: Carbon-saturated Austenite

α: Acicular (Bainitic) Ferrite

γ_{hc}: Carbon-enriched Austenite

At the first stage, part of the austenite transforms into acicular ferrite, and during this transformation, the remaining part of it gets enriched in carbon as the carbon is partitioned from the ferrite phase into the surrounding austenite phase.[43,44] To elaborate this process, nucleation of bainitic ferrite starts at austenite grain

boundaries, and its growth mechanism is displacive. It's important to note that for a displacive transformation to occur, the transformation temperature must be below T_0. T_0 is the temperature at which two different phases (in this case, ferrite and austenite) with identical chemical compositions have the same molar Gibbs free energy. During growth, ferrite plates apply shear strain to surrounding austenite matrix and that causes an increase in dislocation density in these regions, and when glissile dislocations in the growing ferrite phase turn into sessile dislocation by encountering these high dislocation density regions, the growth of the plate stops. The plates partition their excess carbon into the surrounding austenite phase and a new ferrite plate starts to grow from this carbon-enriched austenite phase. This reaction keeps taking place until the carbon concentration of austenite reaches the T_0 curve (Figure 1) beyond which displacive transformation cannot proceed at the corresponding temperature.[35,44,45] This carbon concentration is called C_0. If iron is held at the austempering temperature for relatively long period of times, stage II transformation takes place and carbon-enriched austenite decomposes into carbides and ferrite i.e., completion of bainitic transformation. This causes deterioration of mechanical properties by decreasing ductility, toughness, and fatigue strength.[46–49] For this reason, austempering time at corresponding austempering temperatures should be determined so that the first stage is completed but the second stage transformation has not begun yet. The time interval between the completion of the first stage and the onset of the second stage is called as “processing window” during which the mechanical properties are at their optimum values.[43] Following the completion of the isothermal austempering operation, the iron is quenched to room or lower temperatures. Whether the martensitic formation takes place or not during this cooling operation depends on the stability of the austenite phase obtained after this isothermal austempering process. A representative illustration of the heat treatment route is shared in Figure 2.

After austenitization, achieving a uniform carbon distribution within a fully transformed austenite phase is crucial. This necessitates employment of a sufficiently high austempering temperature to resolve carbides and phosphates and transform all other phases into austenite. However, there is a trade-off: austenitization temperature

affects incubation time and transformation rate during austempering treatment. As the austenitization temperature increases, the incubation time lengthens due to higher carbon content in the austenite phase. As for the transformation rate, it decreases with the increase in austenitization temperature, the reason is that the microstructure present at the beginning of austempering process is affected, including factors such as the number, size, and distribution of the graphite nodules, which strongly impact the transformation kinetics. To elaborate, as the austenitization temperature increases, the number of graphite nodules decreases. That results in an increase in distance between graphite nodules, for this reason, adverse effects take place in transformation kinetics during the austempering process. If the microstructure is relatively refined and homogenous, a greater number of ferrite nuclei form at the beginning of the austempering process.[23–25,50] In addition, a high nodule count with homogeneous distribution contributes to obtaining better mechanical properties.[51] Finally, as for the austenitization time, it depends on the section thickness and initial microstructure. The higher the thickness the more time is required for austenite transformation to take place through the material. For the latter, if the initial microstructure is mostly ferritic, it takes longer than that of a pearlitic matrix[52] Moreover, if the austenitization time is longer than required, it ends up with a relatively coarse austempered structure.[53]

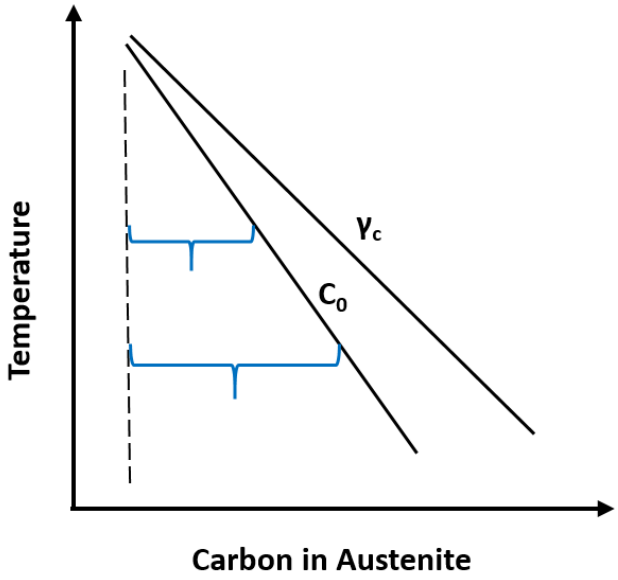

Figure 1. Carbon Concentration in Austenite vs. Temperature (C_0: The Carbon Concentration in Austenite on which the Transformation Ceases at Corresponding Austempering Temperature, γ_c: The Carbon Concentration in Austenite Phase under Equilibrium Conditions)

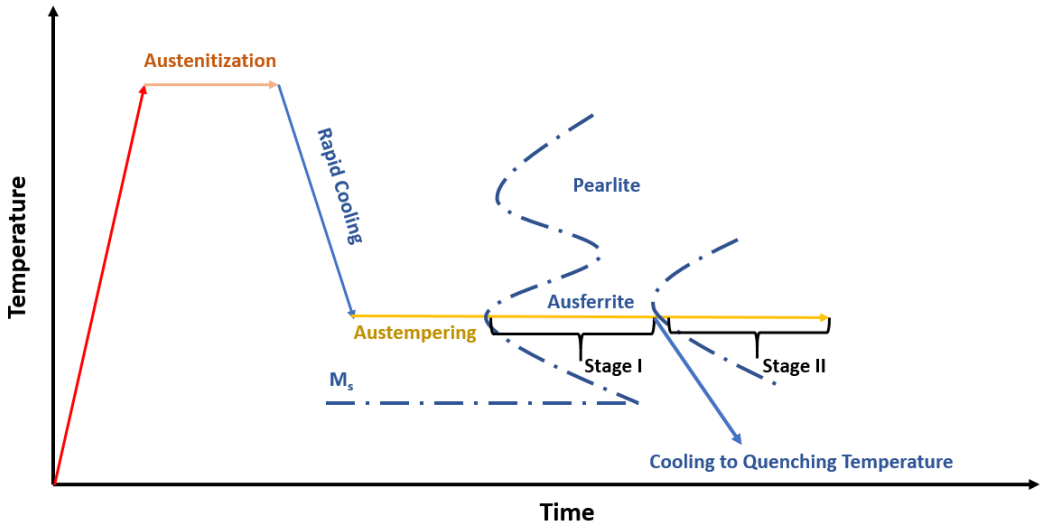

Figure 2. A Representative Illustration of the Heat Treatment Process

As for austempering operation, its parameters have a significant effect on final mechanical properties. Generally, as the austempering temperature increases within an optimal range (typically, 200-450 °C, depending on the material), ductility and toughness properties increase, whereas strength and hardness properties decrease. However, it is crucial to note that austempering outside the optimal range can cause significant decrease in mechanical properties. To be more specific, an austempered ductile iron austempered at between 250 – 350 °C, will have higher strength and hardness but lower toughness and ductility when it is compared to the one austempered at between 350 – 400 °C.[6,14,26] Moreover, at lower temperatures more bainitic ferrite formation takes place due to deviation from the bainite start temperature (B_s) above which no bainite formation takes place.[35] Finally, as expected, at higher temperatures austempering is completed in shorter times[6] and as mentioned earlier, austempering time is very important in terms of obtaining optimum mechanical properties. Therefore, austempering temperature and austempering time should be determined in line with desired mechanical properties to be exhibited by the final product.

1.2 Mechanical Stabilization of Retained Austenite

The use of alloying elements like Silicon and Aluminum in the production of austempered ductile iron promotes the formation and stabilization of retained austenite, leading to an increased amount of retained austenite in the final microstructure. The addition of Silicon, depending on the austempering temperature and time, retards or even prevents the carbide precipitation regarding the nature of bainitic transformation.[33,35] Hence, the surrounding austenite phase is enriched by the released carbon from newly formed ferrite phase and it becomes more stable as it gets enriched in carbon.

As stated, the stability of the retained austenite phase depends on the heat treatment parameters i.e., austempering temperature and time. To elaborate, if the austempering process is held at high temperatures, it results in a relatively low volume fraction of bainite and a large volume fraction of retained austenite with a

bulky volume and a relatively low amount of carbon content. On the other hand, at low temperatures, since the driving force for bainitic transformation is higher, the final microstructure consists of a relatively fine, high-volume fraction of bainite and retained austenite with a relatively high amount of carbon content, rendering it mechanically more stable.[54] Apart from carbon concentration, the morphology of the retained austenite is another criterion for its mechanical stability behavior. Austenite films are much more stable against stress-induced and strain-induced martensite transformation than large austenite blocks. This behavior is simply due to mechanical constriction and strengthening stemming from relatively fine grain size.[44,55,56] In addition, solid solution strengthening also enhances the mechanical stability of retained austenite.[57]

Considering all these factors, it is important to know the stabilization level of retained austenite phase in the microstructure to be able to predict the material's behavior under intended service conditions. In this way, it can be foreseen if the designed material whether the designed material to undergo martensitic or bainitic transformation, as a result of the impacts, stresses or temperature changes to be encountered.

1.2.1 Mechanical Stability Determination

For the concept to be explained, some terms to be utilized are stated below:

M_σ: The lower limit temperature for strain-induced transformation

M_d: The upper limit temperature for strain-induced transformation

M_s: Martensite start temperature

When the temperature is less than Mσ, martensite formation is possible. However, under these conditions, the austenite undergoes only elastic strain. Therefore, the only source of plastic strain comes from the shape deformation of the martensite that forms. For strain-induced transformation to take place, the temperature must be within $M_\sigma \leq T \leq M_d$. In this temperature interval, martensite formation contributes to

achieving maximum elongation by delaying necking onset. As the deformation temperature increases, the austenite phase becomes more stable. However, once M_d is reached, martensite transformation does not occur beyond this temperature. After this point, strain-induced bainite transformation tends to take place.

Hence, the maximum elongation can be achieved when the deformation takes place at just above the M_σ temperature. Due to this characteristic, M_σ can be determined by applying gradual tensile tests on a single specimen at different temperatures. Once $M\sigma$ is reached, the yield profile exhibits a behavior in which an observable drop occurs. This drop arises from the load relaxation due to strain-induced martensite formation.[44] Considering these factors, determination of M_σ temperatures provides an opportunity to interpret the mechanical stabilization behavior of the austenite phase under service conditions.

1.3 Calculation of Phase Diagrams (CALPHAD) Method

For many years now, scientists from all around the world have been working in a collaboration aiming to determine phase diagrams of different material systems by using thermodynamic data. In the late 1960s, computers became a part of the science world, and this development sped up this objective. From then on, both computers have continued to develop and the number of studies on different materials has been added to the database and a more reliable database has emerged. The calculation method based on this living database is called Calphad (CALculation of PHAse Diagrams).[58] As the database has been enriched with reliable studies and the calculation models have been improved, it has become possible to make more accurate calculations over time.[59] Despite the need for further improvements, the CALPHAD (Calculation of Phase Diagram) approach is currently the only applicable way to determine phase diagrams for systems with numerous components.[60]

The Calphad method utilizes a stepwise approach to generate databases for different material systems and simulate the behaviors of multicomponent and multiphase

systems. The main steps of the CALPHAD method are as follows: Firstly, when modeling a property, relevant experimental data including phase equilibria, crystal structure, and thermochemical data are gathered. Secondly, these collected data are critically evaluated in terms of their reliability and consistency. Thirdly, mathematical models are generated employing Gibbs energies to describe the thermodynamic properties of each phase present in the system. Lastly, the binary and ternary systems descriptions are extrapolated to higher-order systems, which allows the calculations of data for more complex systems.[61] By using this method, it is possible to generate thermodynamic and property databases. These can be used for alloying analyses, to get round tons of challenging experiments, and extrapolate to multi-component systems or metastable regions to acquire complete kinetic and thermodynamic properties.[60,62] The CALPHAD approach is widely used in materials science and engineering for an extensive range of applications such as alloy design, phase transformation analysis, and process optimization.[63]

To sum up, to design materials and production processes effectively, having an accurate dataset is a must. Most commercial alloys consist of multiple elements, but the data required for new material or process design is often lacking.[63] Besides, generating the required database by trial-and-error method would be quite costly. At this point, the CALPHAD method provides a solution by creating thermodynamic and property databases and using extrapolation techniques to make required calculations for higher-order systems. In this way, it makes obtaining better material and production process designs eligible. Last but not least, it provides incomparable time savings and cost advantages.

CHAPTER 2

AIM AND MOTIVATION

This study aims to design 2 different austempered ductile irons (ADIs) with superior mechanical properties: One with ultra-high strength and moderate toughness and the other with high strength and high toughness, by employing computational design methods. In the literature, there are no well-accepted values for an ADI to be called ultra-high-strength or high strength. Instead, ADIs are classified by levels based on mechanical properties as per ASTM A897 (Table 1). As for steel, the requirements depend on its classification. For example, according to[64], for commercial structural steel to be considered ultra-high strength, it should have yield strength of at least 1380 MPa. On the other hand, for SSAB[65], the minimum tensile strength should be 780 MPa, while gigapascal steels, as the name states, should exhibit a minimum tensile strength of 1000 MPa. Accordingly, by considering these, for the ADIs aimed to be attained in this study, the former is expected to exhibit tensile strength of at least 1600 MPa, yield strength of 1380 MPa, and impact energy of 35 Joule, whereas for the latter, tensile strength of at least 1000 MPa, yield strength of 700 MPa and impact energy of 100 Joules.

As mentioned earlier, ADI provides an opportunity to obtain excellent mechanical property combinations and it is already in use in several industries. Considering this, if new ADIs with superior mechanical properties, better than the ones already in use, are developed, it is foreseen they can be perfect candidates to replace the existing equivalent materials in several industries since they will offer additional benefits while providing the required mechanical characteristics at the same time. For example, when compared to steel, ADI offers weight and cost advantages, the ability to obtain complex shapes, and generally exhibits less distortion during the production stage.

In line with this objective, the material design process is carried out by tailoring the chemical compositions and heat treatment parameters in view of the literature, and sometimes, making educated guesses based on the previous experimental results. However, as can be deduced from 1.1.1 Parameters Affecting Mechanical Properties section, even a small change in these parameters can significantly affect the final microstructure and, thereby, the mechanical properties. Besides, it is quite costly to determine these parameters just by trial-and-error method. Luckily, in recent years the simulation programs based on the CALPHAD approach have been developed enough to provide an opportunity to determine these parameters without performing lots of experiments. For this reason, in this research, alongside literature and experimental data, these benefits of computational design methods are employed.

CHAPTER 3

COMPUTATIONAL DESIGN PROCESS

For the effective use of computational design, it is essential to establish a specific methodology. Furthermore, this methodology must be verified to confirm its validity and efficiency. Once verified, it becomes possible to conduct a comprehensive examination of the impacts of alloying elements and heat treatment parameters, with the aim of progressively narrowing down the feasible combinations. Within the scope of this study, the specified methodology is employed to design two distinct sets of samples. This approach involves the utilization of the 1st set as a point of reference when specifying the design parameters for the 2nd set. This strategy is motivated by the acknowledgment that computational design tools may not anticipate certain unpredictable factors. Consequently, by evaluating the results of the 1st set, the necessary improvements are implemented in the 2nd set. This chapter presents the computational design methodology, its validation process and results of the computational design processes for the 1st and 2nd sets. The analyses presented in this chapter are conducted by utilizing Thermocalc Software.

3.1 The Computational Design Methodology and Its Verification

As mentioned in earlier sections, the chemical composition and heat treatment parameters are intended to be designed by using computational methods via the software based on the Calphad Approach. To validate this methodology, a comparison is made between the results obtained from Thermocalc Software and experimental data from three ADI samples with known chemical compositions and heat treatment parameters. This sample set includes 2 different chemical compositions, namely V1 and V2, and 2 different heat treatment scenarios with varying austempering temperatures and times. The samples are named with respect

to their chemical compositions and austempering parameters. The chemical compositions and heat treatment parameters are given in Table 2.

Table 2. Chemical Compositions and Heat Treatment Parameters of Validation Samples

Sample Name	C (wt. %)	Si (wt. %)	Mn (wt. %)	Cu (wt. %)	Austenitization Temp. (ºC)	Austenitization Time (Min.)	Austempering Temp. (ºC)	Austempering Time (Min.)
V1-350/90	3.6	2.5	0.35	0.0	925	60	350	90
V1-400/120	3.6	2.5	0.35	0.0	925	60	400	120
V2-350/90	3.6	2.5	0.35	0.8	925	60	350	90

In the first step, the volume fractions of all the phases across a wide temperature range are examined to identify the phases present in this range and determine their respective fractions. These graphs for V1 and V2 are given in Figure 3 and 4, respectively. The percentages of the phases present before the heat treatment processes for each sample are shared in Table 3. The values in the first section are calculated by using Thermocalc Software, whereas the ones in the second section are the experimental results. When examining the percentages of graphite and alpha phase, it is observed that the Thermocalc calculations are quite consistent with the experimental results.

Table 3. The Phase Percentages in As-Cast State – Validation Samples

Before Heat Treatment (As-Cast)	**V1**	**V1**	**V2**
Thermocalc Calculations			
Graphite (vol.%)	11.1	11.1	11.1
Alpha Phase (vol.%)	88.9	88.9	88.9
Experimental Results			
Graphite (vol.%)	11.6 ± 0.3	11.2 ± 0.3	11.0 ± 0.4
Alpha Phase (vol.%)	88.4 ± 0.3	88.8 ± 0.3	89.0 ± 0.4

In following steps, the TTT diagrams (Figure 5 and 6) are drawn by setting the equilibrium conditions at the corresponding austenitization temperatures on relevant property models. By looking at these diagrams, the austempering temperatures specified for each sample are above the Ms temperatures as required. To calculate the transformation completion times at the corresponding austempering temperatures, it is decided to employ Johnson-Mehl-Avrami-Kolmogorov (JMAK) Equation[66] (Equation 1). However, JMAK equation has certain assumptions and some of them are not met in case of bainitic transformation. For example, one of these assumptions includes that nucleation takes place randomly and homogeneously over the entire volume. In bainitic transformation, nucleation takes place preferentially at grain boundaries which is contrary to the assumption of random and homogeneous nucleation in the JMAK equation. Furthermore, this equation is used for phase transformations involving diffusion of atoms across phase interfaces, but growth mechanism of bainitic transformation is displacive. Yet carbon partitioning takes place from ferrite plates into surrounding austenite phase. Although some of these assumptions are not exactly valid in the case of bainitic transformation, it can still be employed to attain a simplified description for bainitic transformation kinetics, as long as the limitations are acknowledged and considered. Besides, so far, there has been no other model which is more accepted than the JMAK equation for bainitic transformation. In this context, in the literature, there are studies in which

JMAK equation is used to describe the bainitic transformation kinetics both in steel and ADI materials.[66–70]

$$Y = 1 - \exp[-k(t)^n] \quad \text{(Equation-1)}$$

Y = Volume Fraction **k** = Rate Constant **t** = Time **n** = JMAK Exponent

To calculate the transformation completion times, it is necessary to first obtain the constant parameters in the JMAK equation. To do so, at least two pairs of volume fraction and time data are needed. In this context, 2% and 50% bainitic transformation times are derived from the corresponding TTT curves. However, 50% bainite transformation does not occur in all three samples at their corresponding austempering temperatures. Unfortunately, any other time data regarding any other percentage of bainite transformation cannot be obtained via Thermocalc Software, Consequently, the relevant completion times for bainite transformations cannot be calculated. Nonetheless, considering that the transformation rate is highly temperature-dependent, and given that the austempering operations are taken place at relatively higher temperatures for all samples, it is reasonable to assume that the prescribed austempering times to be adequate for the completion of the bainite transformation. For the samples to be designed within the scope of this study, it is anticipated that 50% bainitic transformation will readily occur, making JMAK calculations applicable.

While calculating the final phase percentages, some assumptions are made. Firstly, during the analyses, the austenitization times are found to be far more than sufficient for graphite nodules to reach equilibrium conditions for all the samples. For this reason, it is assumed that graphite nodules form and maintain a constant volume percentage under equilibrium conditions at corresponding austenitization temperatures throughout all subsequent operations. Secondly, as mentioned above, the austempering times are sufficient for the bainite phases to form and reach equilibrium conditions at the relevant austempering temperatures. Thirdly, C_0 compositions of carbon at corresponding austempering temperatures are obtained and new systems having those amounts of carbon contents are defined. As for the

other elements, since only carbon partitioning occurs, and the growth mechanism is displacive, their fractions are assumed to be the same as those present in the austenite phase under equilibrium conditions at the corresponding austenitization temperatures. Subsequently, martensite start temperatures and martensite fractions are calculated based on these new compositions. Retained austenite percentages are then determined using these martensite fractions at 0°C (quenching temperature) and the retained austenite fractions obtained after the completion of the bainitic transformation at the corresponding austempering temperatures.

For all three samples, martensite start temperatures are higher than the quenching temperature. Therefore, it is anticipated that some austenite to be transformed into martensite during the cooling process to 0°C. The results of these calculations are presented in Table 4. Similar to what is displayed in Table 3, the first section presents Thermocalc calculations, while the second section provides experimental results. Since only the retained austenite and graphite phases are experimentally measured (Section 4.1), the volume percentages of the martensite and ferrite phases are given together as remaining phases in the microstructure.

Table 4. The Phase Percentages After the Heat Treatments – Validation Samples

After Heat Treatment Process (Final State)	**V1-350/90**	**V1-400/120**	**V2-350/90**
Thermocalc Calculations			
Graphite (vol.%)	8.7	8.7	8.8
Martensite + Ferrite (vol.%)	52.3	64.9	54.2
Retained Austenite (vol%)	39.0	26.5	36.9
Experimental Results			
Graphite (vol.%)	8.6 ± 0.3	10.2 ± 0.6	7.4 ± 0.7
Martensite + Ferrite (vol.%)	53.8 ± 1.8	60.7 ± 2.3	62.5 ± 4.1
Retained Austenite (vol.%)	37.6 ± 1.5	29.1 ± 1.7	30.1 ± 3.4

In Table 4, given the reliability of these results, it is evident that the intended computational design methodology can be effectively employed within the scope of this study.

All the analyses presented in this section are conducted by employing TCFE11 (Steels/Fe-Alloys v11.0) and MODFE6 (Steels/Fe-Alloys v6.0) databases.

After verifying the computational design methodology, a detailed examination of the impact of each alloying element and heat treatment parameters, including temperature and time of austenitization and austempering treatments, and quenching temperature, is conducted. These production parameters are specified to obtain different microstructures in terms of volume percentages and morphologies of the phases, to be able to determine the effect of these variables on mechanical properties. In line with this, final microstructures are aimed to consist of ausferrite structures with different sizes, different amounts of retained austenite having different stability levels, and graphite nodules with high nodularity and nodule count. The details regarding this examination process are shared in 5.1 "Computational Design Considerations" section. As previously mentioned, to combine educated assumptions with actual experimental data, integrated heat treatment and alloy design processes are conducted successively for two distinct sets. The details of these processes are described in 3.2 "Computational Design of the 1st Set" and 3.3 "Computational Design of the 2nd Set" sections. The outcomes of these processes are compared with the experimental results: the consistencies, discrepancies, and mechanical test results are subsequently discussed in Chapter 5 "Results and Discussion".

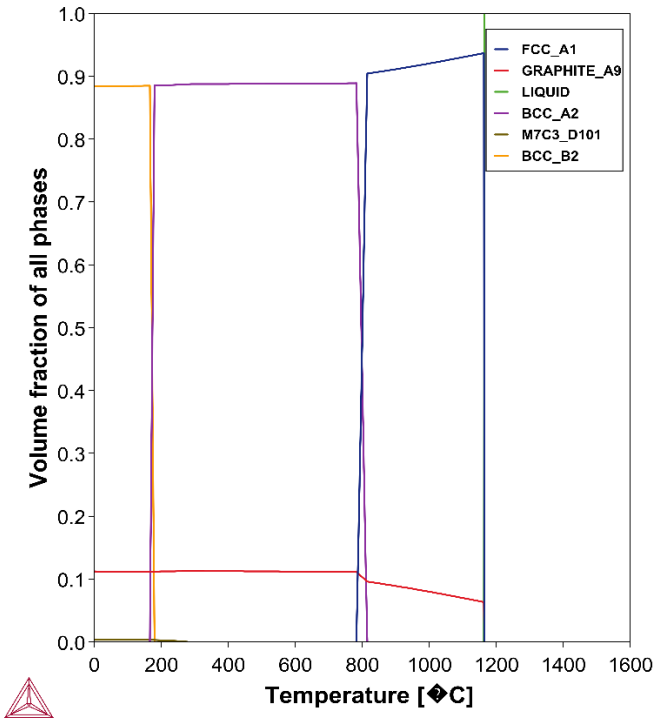

Figure 3. V1 - Volume Fractions of the Phases Under Equilibrium Conditions with Respect to Temperature

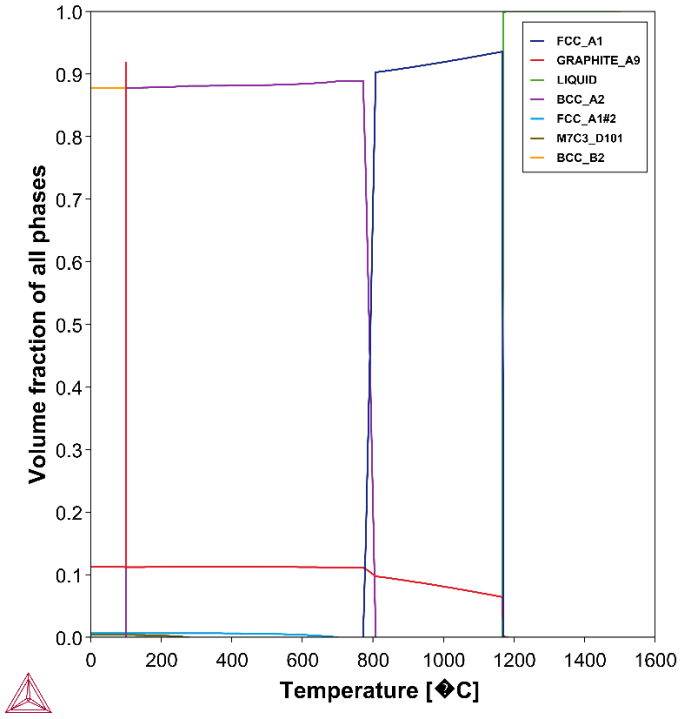

Figure 4. V2 - Volume Fractions of the Phases Under Equilibrium Conditions with Respect to Temperature

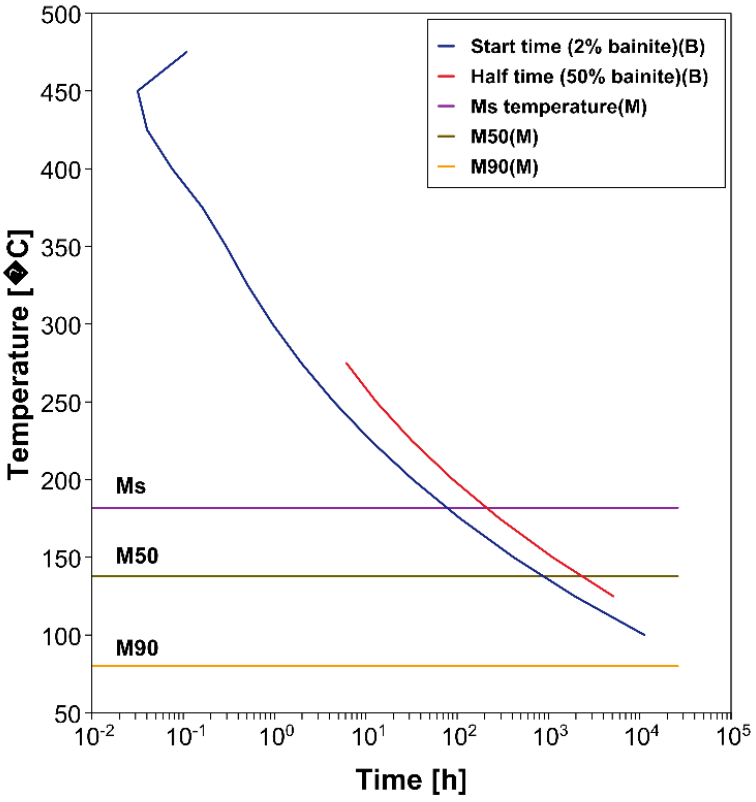

Figure 5. V1 - TTT Diagram

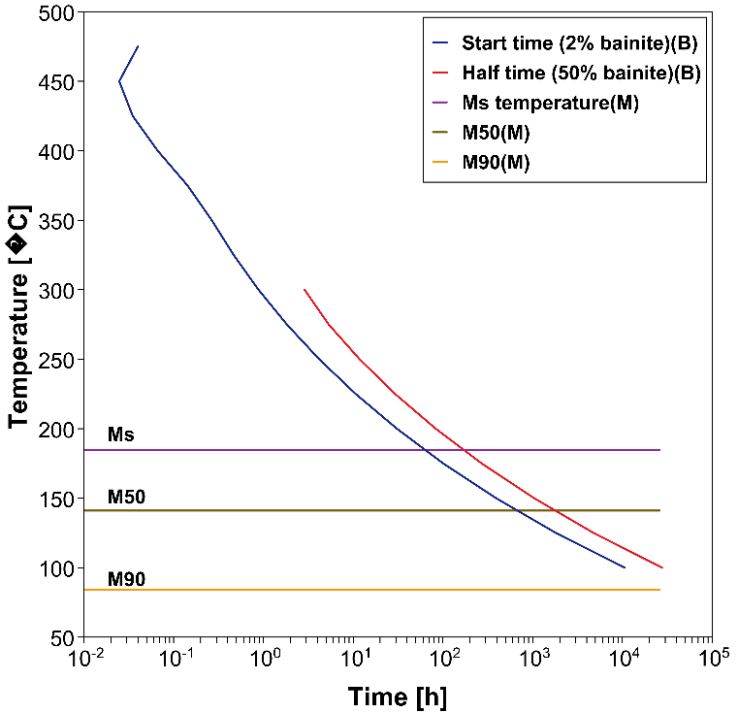

Figure 6. V2 - TTT Diagram

3.2 Computational Design of the 1st Set

Considering all the facts mentioned in 5.1 "Computational Design Considerations" section, the 1st set is specified in a way consisting of 4 samples with 2 different chemical compositions and 2 different heat treatments. One of these chemical compositions is Al-based, named Alloy X, whereas the other one is Ni-based, named Alloy Y. Alloy X contains 1 wt.% Aluminum, and Alloy Y does 1 wt.% Ni. For Alloy-X and Alloy-Y, graphs showing the volume percentages of all phases at equilibrium conditions within 0-1500 °C are shared in Figure 7 and 8, respectively. The heat treatment details are presented in Table 5. The pre-treatment specified in the table refers to a common process which is carried out for all samples before any of the two heat treatment scenarios. The samples are named with respect to their chemical compositions, heat treatments and austempering parameters, respectively, given in Table 5.

Table 5. The Heat Treatment Processes of the 1st Set

Alloy	Heat Treatment	Sample Name	Steps
	Pre-treatment	**Common Process**	1. Homogenization for 2 hours at 1050 °C 2. Furnace Cooling to 850 °C 3. Austenitization for 1 hour at 850 °C
Alloy X (1 wt.% Al)	**Heat Treatment 1**	**X1-250/24** **Y1-250/24**	1. Austempering for 24 hours at 250 °C 2. Cooling in iced water 3. Cooling in dry ice (-65 °C) 4. Tempering for 2 hours at 180 °C 5. Air cooling to R.T.
Alloy Y (1 wt.% Ni)	**Heat Treatment 2**	**X2-350/2** **Y2-350/2**	1. Austempering for 2 hours at 350 °C 2. Cooling in iced water 3. Tempering for 2 hours at 180 °C 4. Air cooling to R.T.

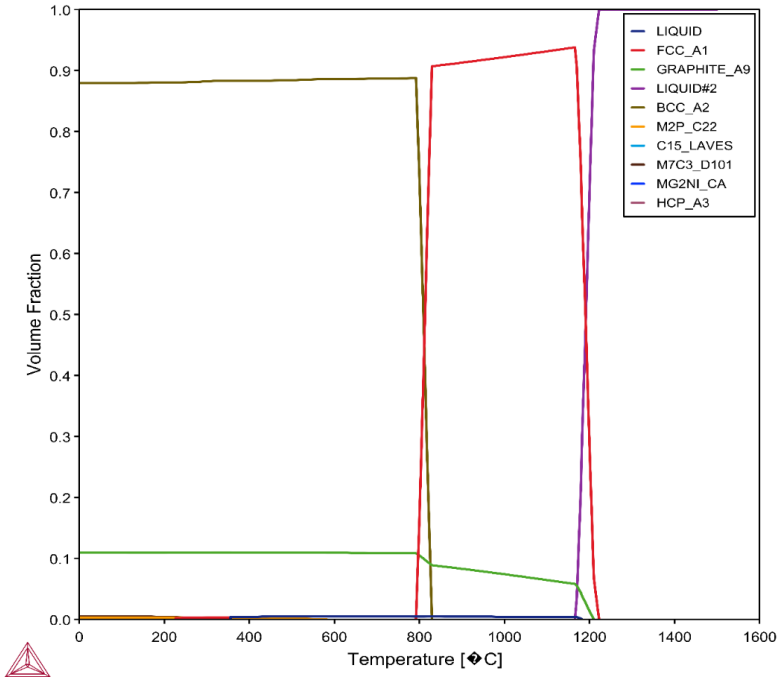

Figure 7. Alloy X - Volume Fractions of the Phases Under Equilibrium Conditions with Respect to Temperature

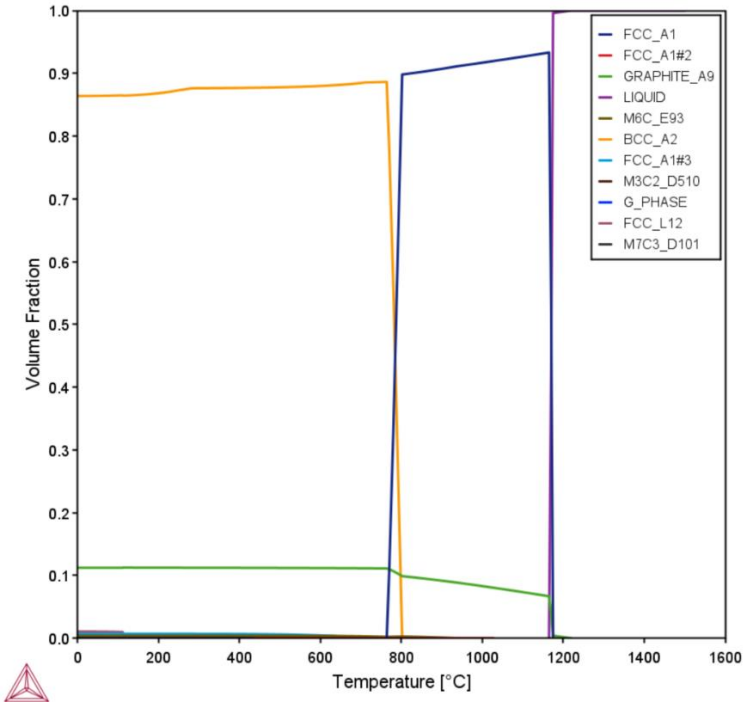

Figure 8. Alloy Y - Volume Fractions of the Phases Under Equilibrium Conditions with Respect to Temperature

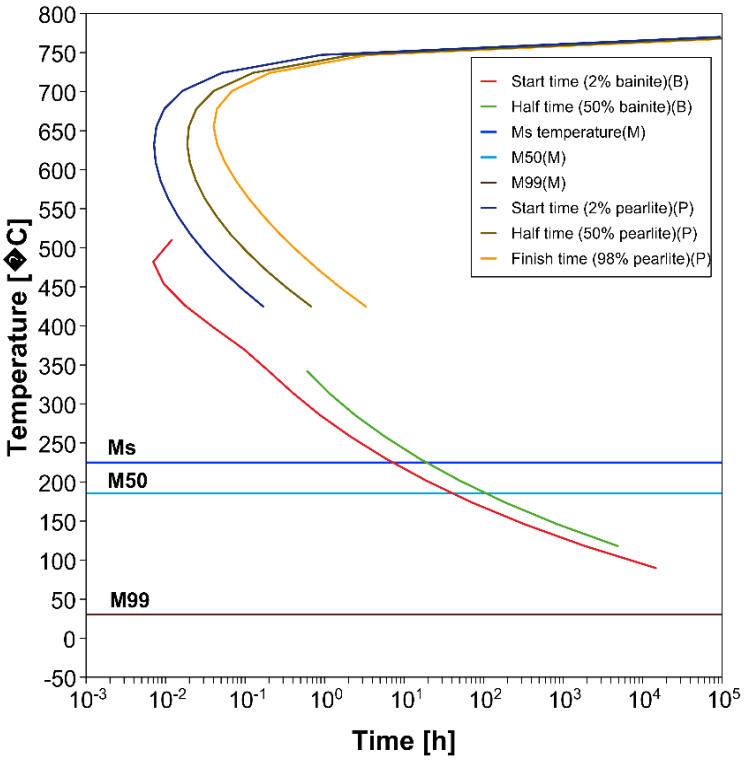

Figure 9. Alloy X - TTT Diagram

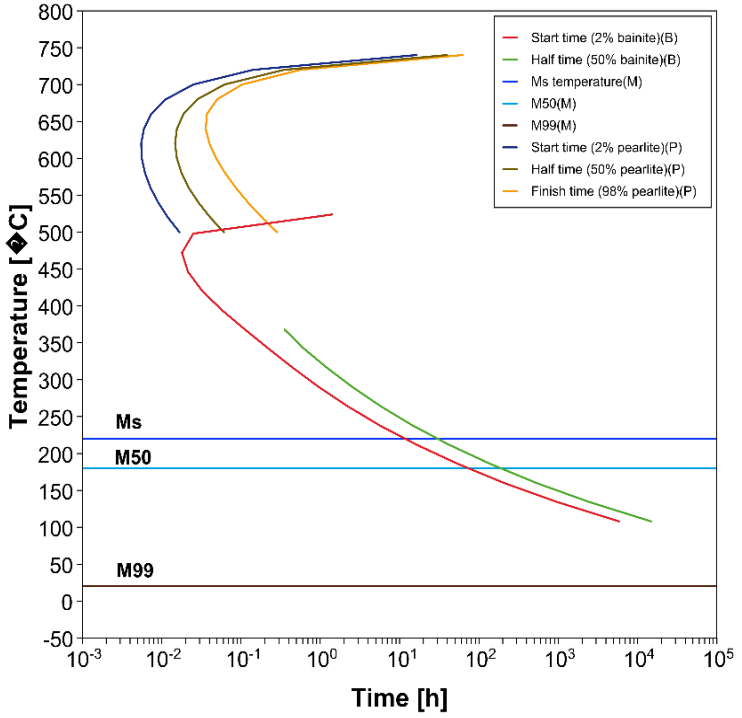

Figure 10. Alloy Y - TTT Diagram

TTT diagrams are drawn and shared in Figure 9 and 10. The times required to complete the bainitic transformation during austempering treatments conducted at 250 °C and 350 °C are calculated by using the values obtained from the TTT diagrams (2% and 50% bainite transformation times), the JMAK Equation and bainite volume fractions under equilibrium conditions at the corresponding austempering temperatures. The results are presented in Table 6. As indicated by the data in Table 5 and Table 6, the austempering times specified in all heat treatment scenarios are sufficient for the bainite phases to reach the equilibrium conditions. Moreover, as demonstrated in Figures 11 and 12, the alloy compositions are effectively designed to prevent carbide formation during austempering treatments for both alloys.

Table 6. Bainitic Transformation Completion Times - The 1st Set of Samples

Sample Name	**Completion Time (Min.)**
X1-250/24	494
Y1-250/24	636
X2-350/2	31
Y2-350/2	33

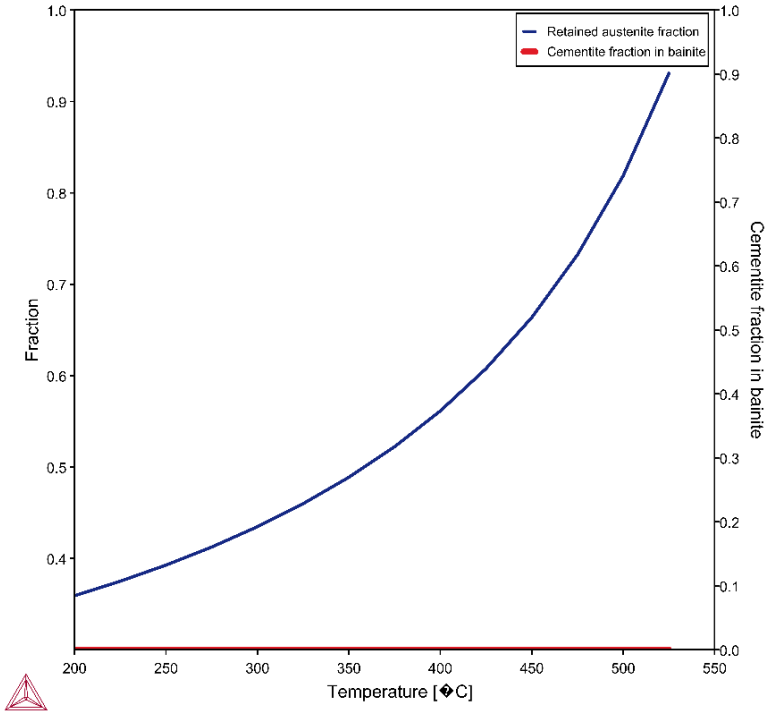

Figure 11. Alloy X - Retained Austenite and Cementite Fractions with Respect to Austempering Temperature

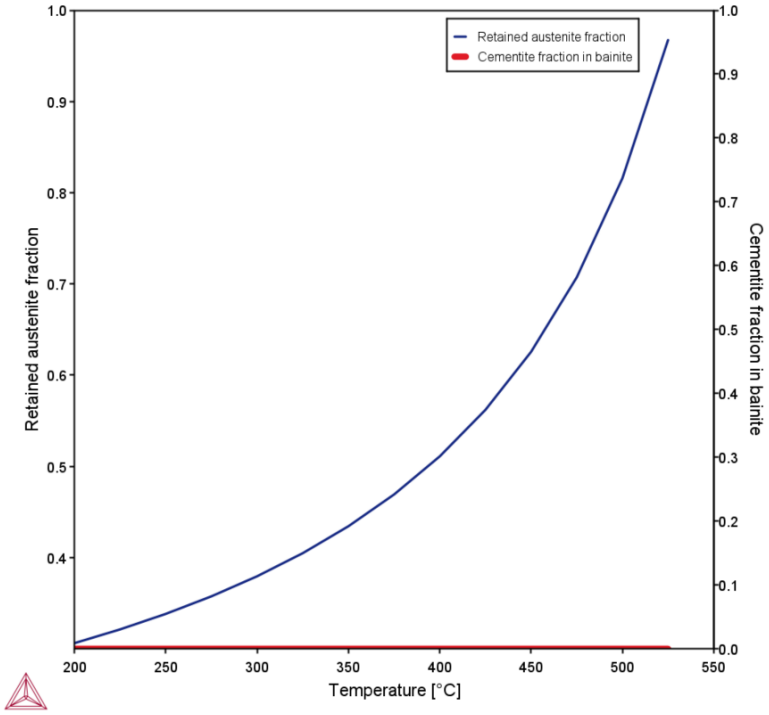

Figure 12. Alloy Y - Retained Austenite and Cementite Fractions with Respect to Austempering Temperature

When calculating the retained austenite volume percentages in the final microstructures, the same methodology described in the previous section is applied. The results are given in Table 7.

All the analyses presented in this section are carried out by employing TCFE11 (Steels/Fe-Alloys v11.0) and MODFE6 (Steels/Fe-Alloys v6.0) databases.

Table 7. Calculated Retained Austenite Percentages – The 1st Set of Samples

Sample Name	Retained Austenite (vol.%)
X1-250/24	15.7
Y1-250/24	19.8
X2-350/2	19.9
Y2-350/2	21.0

3.3 Computational Design of the 2nd Set

Based on the results of the 1st set, discussed in Chapter 5, new heat treatment processes and alloy compositions are determined through additional computational analyses. In line with this, it is decided to keep with Alloy Y and additionally, its variant containing 2 wt.% Ni instead of 1 wt.%, named Alloy Z. The new heat treatment processes are presented in Table 8. Just like in the 1st set, the samples are named with respect to their chemical compositions, heat treatments and austempering parameters, respectively, given in Table 8.

Table 8. The Heat Treatment Processes of the 2nd Set

Alloy	Heat Treatment	Sample Name	Steps
Alloy Y (1 wt.% Ni)	**Heat Treatment 3**	**Y3-350/2**	1. Austenitization for 2 hours at 920 °C 2. Austempering for 2 hours at 350 °C 3. Cooling in iced water 4. Tempering for 2 hours at 180 °C 5. Cooling in iced water
	Heat Treatment 4	**Y4-250/24**	1. Austenitization for 2 hours at 920 °C 2. Austempering for 24 hours at 250 °C 3. Cooling in iced water
Alloy Z (2 wt.% Ni)	**Heat Treatment 5**	**Z5-350/3**	1. Austenitization for 2 hours at 920 °C 2. Austempering for 3 hours at 350 °C 3. Cooling down to R.T. 4. Cooling in iced water
	Heat Treatment 6	**Z6-225/36**	1. Austenitization for 2 hours at 920°C 2. Austempering for 36 hours at 225 °C 3. Cooling down to R.T. 4. Cooling in iced water

For Alloy Y and Alloy Z, the graphs showing the volume percentages of the phases at equilibrium conditions within 0-1500 °C are shared in Figure 13 and 14, respectively. TTT diagrams are drawn for each alloy and shared in Figure 15 and 16.

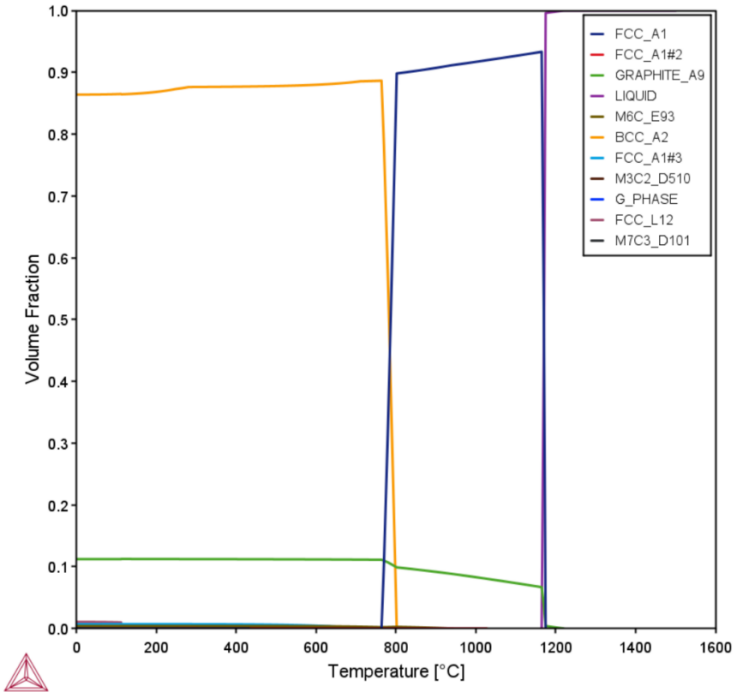

Figure 13. Alloy Y - Volume Percentages of the Phases Under Equilibrium Conditions with Respect to Temperature

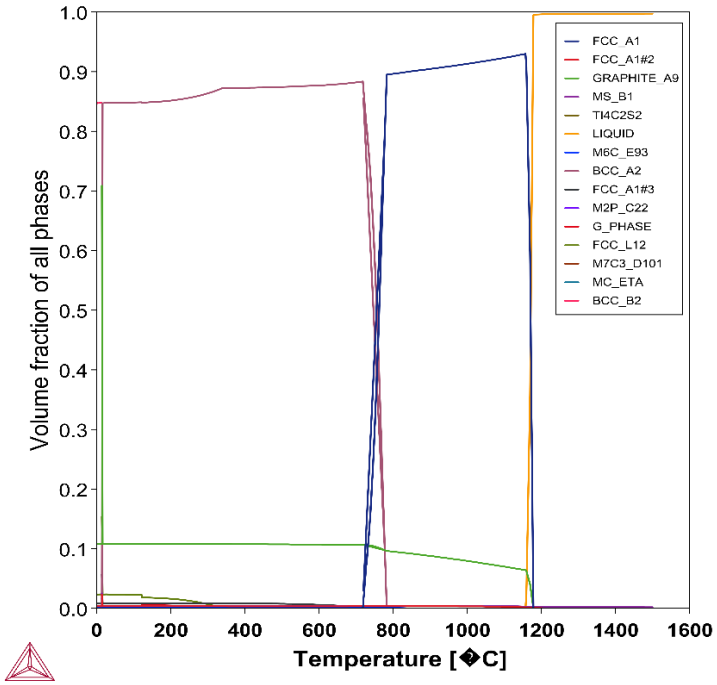

Figure 14. Alloy Z - Volume Percentages of the Phases Under Equilibrium Conditions with Respect to Temperature

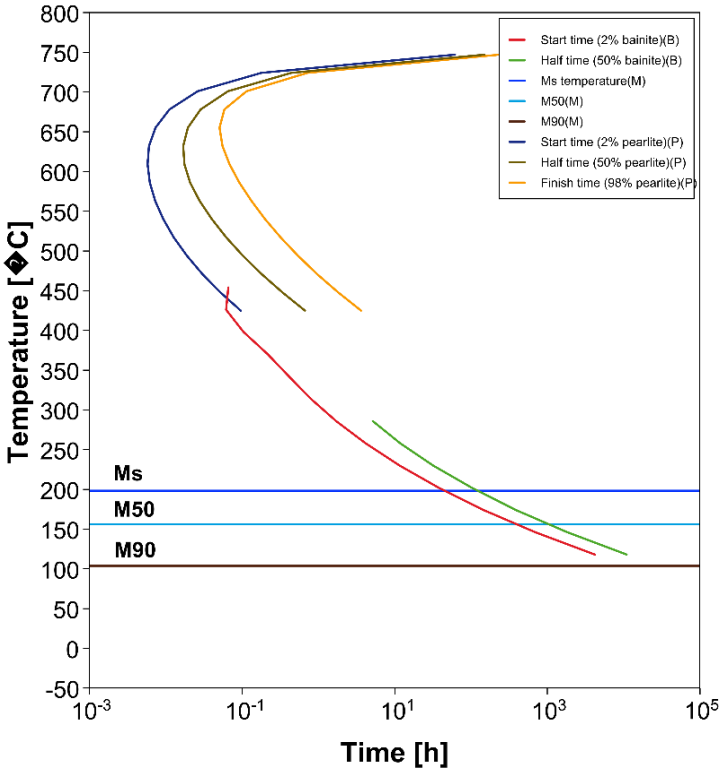

Figure 15. Alloy Y – TTT Diagram

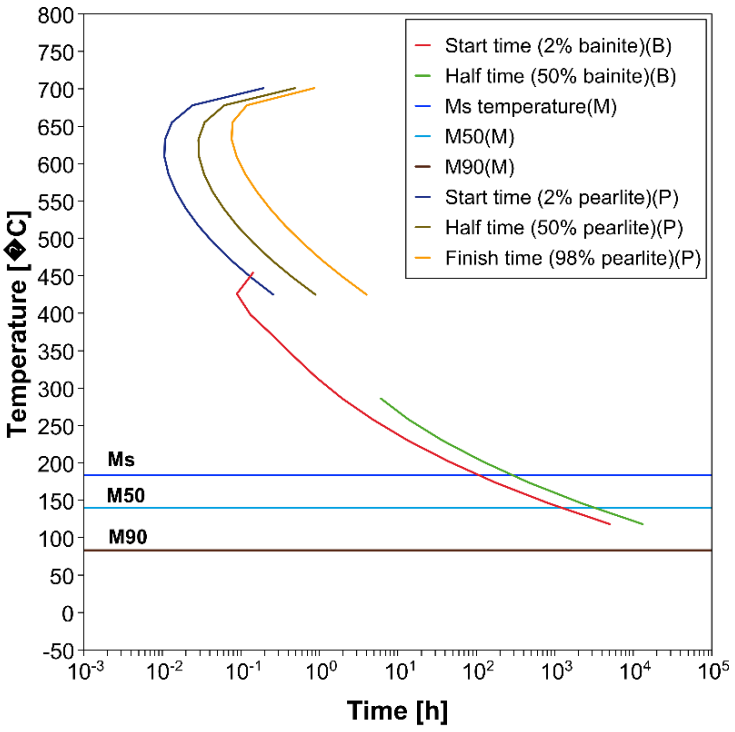

Figure 16. Alloy Z – TTT Diagram

As for the austempering treatments, the times required to complete the bainitic transformation at 225 °C, 250 °C, and 350 °C are calculated. The calculations are made by using the same way in the 1st Set (in 3.1 section). Since 50% bainite transformation does not occur for both alloys at 350 °C and any other time data regarding the bainite transformation cannot be obtained via Thermocalc Software, the relevant completion times for bainite transformations cannot be calculated. In any case, considering that the transformation rate is highly temperature-dependent, and given that the austempering operation is taken place at a relatively high temperature of 350 °C, it is reasonable to assume that the specified austempering times to be sufficient for the full completion of the bainite transformations. The results are presented in Table 9.

As seen in Table 9, 36 hours of austempering time is not enough for the completion of bainitic transformation for Z6-225/36, however, this time is specified intentionally to attain the desired amount of retained austenite. To calculate the final retained austenite percentage, the volume percentage of bainite formed within 36 hours of austempering is calculated by using the JMAK equation. Subsequently, the lever rule is applied to obtain carbon content in the austenite phase at the end of 36 hours. Chang has demonstrated that the retained austenite percentage can be calculated by applying the lever rule if the initial and final carbon content in it is known[71], so this should be applicable vice versa. In all reasons, the value will eventually be between the carbon content present just after the austenitization and the C_0 values. After applying the lever rule and obtaining the carbon fraction in austenite, the same methodology, described in 3.1 section, is applied to calculate the volume percentage of the retained austenite phase in the final microstructures. The results are given in Table 10. Moreover, as demonstrated in Figure 17 and 18, alloying compositions are appropriately designed for both alloys to prevent carbide formation during the austempering treatments.

All the analyses presented in this section are carried out by employing TCFE12 (Steels/Fe-Alloys v12.0) and MODFE7 (Steels/Fe-Alloys v7.0) databases.

Table 9. Bainitic Transformation Completion Times - The 2nd Set of Samples

Sample Name	Completion Time (Min.)
Z6-225/36	2881
Y4-250/24	970
Y3-350/2	N/A
Z5-350/3	N/A

Table 10. Calculated Retained Austenite Volume Percentages – The 2nd Set of Samples

Sample Name	Retained Austenite (vol.%)
Y3-350/2	25.9
Y4-250/24	40.1
Z5-350/3	41.1
Z6-225/36	21.8

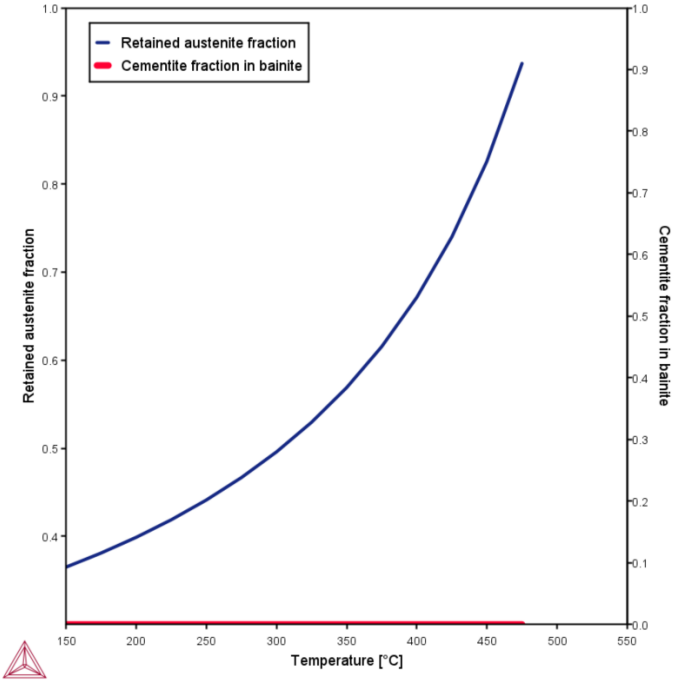

Figure 17. Alloy Y - Retained Austenite and Cementite Fraction with Respect to Austempering Temperature

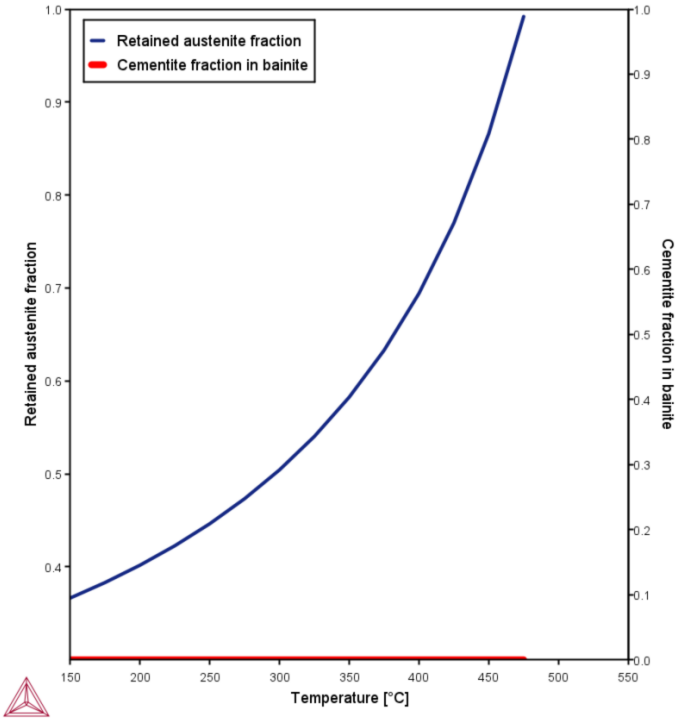

Figure 18. Alloy Z - Retained Austenite and Cementite Fraction with Respect to Austempering Temperature

CHAPTER 4

EXPERIMENTAL PROCEDURE

This chapter presents a comprehensive overview of the experimental procedures for producing and characterizing the validation samples, the 1st set of samples, and the 2nd set of samples. It includes detailed descriptions of the production stages, microstructural analysis methods, and mechanical testing methods.

4.1 Validation Samples

The samples used to validate the computational design methodology are initially cast as Y-blocks. Two different chemical compositions, V1 and V2, are used in the casting process, resulting in three samples: two castings of V1 and one casting of V2. These castings undergo the heat treatment processes listed in Table 2 using Gleeble 3500. The heat treatment processes are also depicted in Figure 19.

Following the heat treatment processes, in accordance with ASTM E3[72], metallographic preparations are conducted as follows: a two-step grinding process using sandpapers with grit sizes of 320 and 500, respectively, and a three-step polishing process using diamond paste with particle sizes of 9μ, 3μ, and 1μ, respectively. Subsequently, a total of 30 images are captured at 50x magnification using a Nikon Eclipse LV 150 optical microscope, under bright field illumination to characterize the graphite particles. The nodularity analyses are conducted by using Clemex Vision Pro software, in accordance with ASTM E2567[73]. However, within the scope of this study, these nodularity analyses are utilized just for the determination of graphite volume percentages. The results for the as-cast and the heat-treated samples are presented in Table 3 and Table 4, respectively.

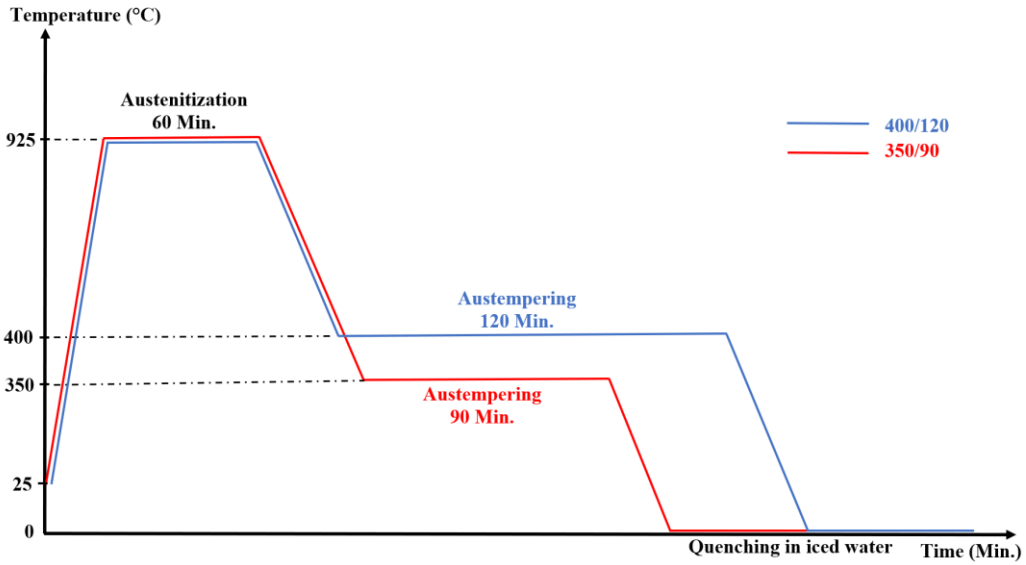

Figure 19. Heat Treatment Routes for Validation Samples

Finally, retained austenite measurements are carried out utilizing EBSD analyses. Before these analyses, an additional polishing process using oxide polishing suspension is applied. These analyses are performed by means of a Zeiss Merlin field emission gun scanning electron microscope, equipped with an EDAX/TSL EBSD system and a Hikari EBSD camera. The following key parameters are applied for optimization:

- Accelerating voltage: 15 kV
- Beam current: 6.0 nA
- Working distance: 13 mm
- EBSD data acquisition: EBSD maps are measured on a hexagonal grid with a step size of 50 nm.

The EBSD camera is operated at a frame rate of 100 frames per second with an exposure time of 10 ms. Additionally, binning is applied at a 4×4 configuration (160×120 pixels). To ensure reliability, it is implemented a grain confidence index standardization method by applying a minimum CI filter of 0.1. The volume percentages of the retained austenite phases for each sample are shared in Table 4.

4.2 The 1st Set of Samples

The casting process is carried out by preparing the castings with a determined chemical composition and melting them in an induction furnace with a capacity of 100 kg. The melts are superheated above 1500 °C and the required alloying elements are added into it. The amounts of the elements are adjusted by means of a spectrometer. Afterwards, the melts are cast into Y-block-shaped green-sand molds as per EN 1563:2018 Spherical Graphite Cast Iron Standard[74]. The as-cast microstructures are investigated by means of a Leica DM 2700 optical microscope and shared in Figure 23 and 24. The metallographic sample belonging to Alloy X is etched with 3% Nital solution, whereas that of Alloy Y is etched with 6% Nital solution.

Nodularity analyses of the as-cast samples are carried out according to ASTM E112/E1382 standard. Approximately 300 images are acquired by using motorized surface scanning at 500x magnification from the best focal point of the samples, and the calculations are made by employing ImageJ Software. The results are presented in Table 11.

Following the completion of the microstructural investigations on the as-cast samples, the Y blocks are subjected to corresponding heat treatment processes specified in Table 5. The heat treatment processes are depicted also in Figure 20. Homogenization and austenitization processes are carried out in an austenitization furnace with a volume of 140.000 mm^3. Afterwards, the blocks are moved into a salt bath containing 1.5-ton AS135 standard salt with 130 mm of diameter for austempering operation.

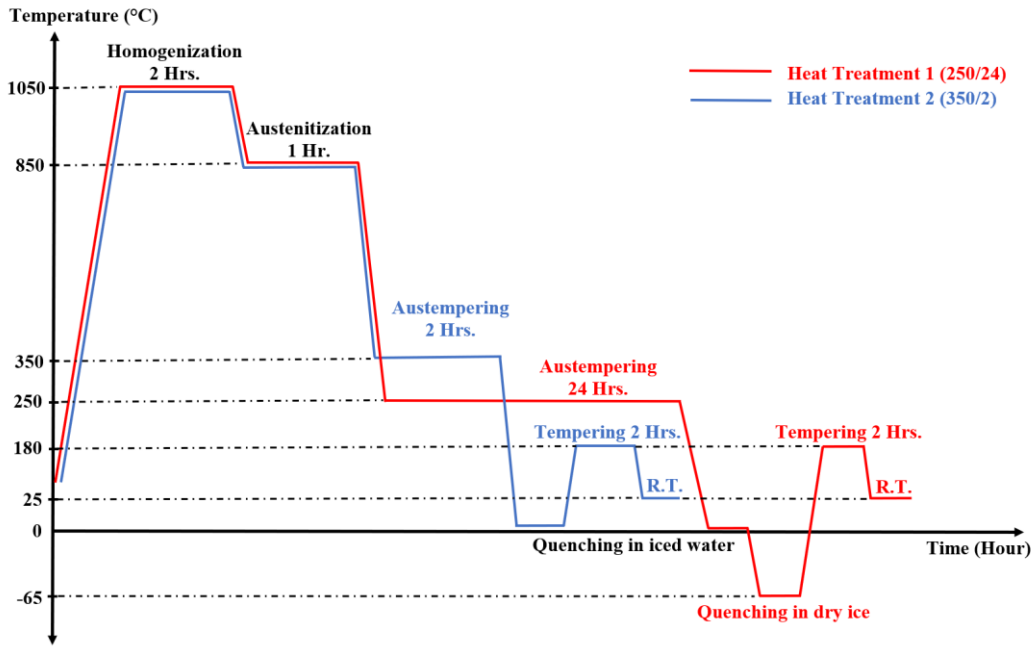

Figure 20. Heat Treatment Routes for the 1st Set of Samples

After performing the heat treatment processes, the Y-blocks are cut from their bottom to obtain the specimens with the appropriate dimensions required for mechanical tests in accordance with EN 1563 Standard[74]. For each heat treatment process, 3 tensile samples and 4 unnotched impact test samples are prepared. These samples are given in Figure 21. These specimens are subjected to impact tests at 25 °C, Brinell hardness, and tensile tests to determine their mechanical performances. Hardness values are measured by means of a BMS (Bulut Makina Sanayi) brand Brinell hardness measuring device. Measurements are carried out with a 10 mm diameter ball at a load of 3000 kgf, in accordance with the EN-ISO 6506 standard as per HB10 method. The samples are ground with 180-grit sandpaper from the lower and upper surfaces prior to the measurements. The average values of the hardness measurements from 5 different points are calculated for each sample. As for tensile tests, they are applied by using ZWICK ROEL Z250 with a capacity of 250 kN in accordance with EN ISO 6892-1 standard.[75] The speed is adjusted as 0.0067 mm/s. Finally, impact tests are performed by means of an ALŞA brand of impact test equipment, which can apply 300 Joule of impact energy at maximum, at 25 °C.

Results of these mechanical tests are shared in Table 12 and Figure 29. The values for the tensile tests represent the average of the 3 different tests, whereas the impact test results are the average value of the highest 3 out of 4 different results. As for Brinell hardness values, they are the average of the measurements taken from 5 different points of each sample.

Figure 21. Tensile and Impact Test Samples

Metallographic samples are mounted in bakelite and ground with 1200 μm and 2500 μm grit sandpapers, respectively. Then, they are polished with 3 μm and 1 μm diamond suspensions, respectively. Afterwards, the polished samples are etched with 3% nital solution and their microstructures are examined by means of a Leica DM 2700 optical microscope. The microstructures captured are shared in Figure 25, 26, 27, and 28.

The volume percentage of the retained austenite phases are measured using Stresstech G2R X-Stress 3000 XRD equipment. The determination is made with Cr X-ray tube in accordance with ASTM E975 Standard Practice for X-ray Determination of Retained Austenite in Steel with Near Random Crystallographic Orientation[76]. The intensities of the peaks used for the ferrite phase are 106 and 156 and 80 and 130 for austenite. The results are shared in Table 13.

4.3 The 2nd Set of Samples

Just as in the 1st Set, Alloy Y and Alloy Z are cast as Y-blocks in accordance with EN 1563:2018[74]. Their as-cast microstructures captured by means of a Leica DM 2700 optical microscope are shared in Figure 31. The metallographic sample belonging to Alloy Y is etched with 6% Nital solution, whereas that of Alloy Z is etched with 3% Nital solution.

Nodularity analysis is conducted by using the same methodology as in the 1st set (section 4.2). Nodularity percentages and nodule counts are shared in Table 16.

For each heat treatment process, the Y blocks are subjected to the corresponding heat treatment processes stated in Table 8. The heat treatment processes are depicted also in Figure 22. The austenitization and austempering processes are performed by using the same equipment and under the same conditions detailed in the previous section (section 4.2).

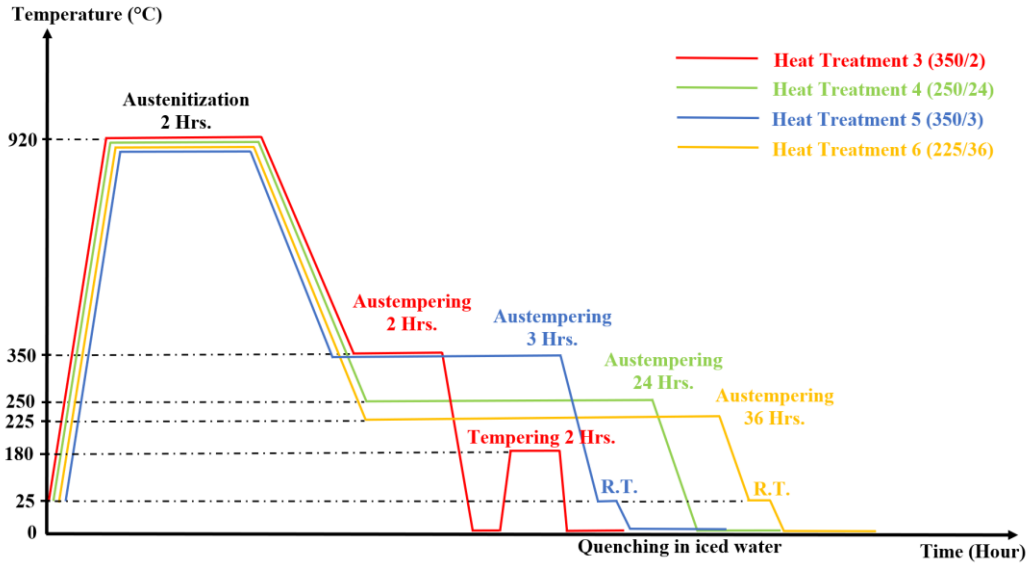

Figure 22. Heat Treatment Routes for the 2nd Set of Samples

After applying the heat treatment processes, Y blocks are cut along the central axis from their lower regions as per EN 1563 Standard[74] and machined to obtain specimens with the appropriate dimensions required for mechanical tests. At this stage, just as in the 1st set, 3 tensile and 4 unnotched impact test specimens are prepared. These specimens are subjected to identical tests as those in the 1st set (section 4.2) and the values are calculated by using the same methodology. The results are shared in Table 17.

Metallographic samples are prepared by following the same steps for those in the 1st set (section 4.2) and their microstructures are examined by means of a Leica DM 2700 optical microscope. The microstructures are shared in Figure 32, 33, 34, and 35.

For the retained austenite measurements, the same equipment and methodology used for the 1st set (section 4.2) are employed. The results are presented in Table 18.

CHAPTER 5

RESULTS AND DISCUSSION

5.1 Computational Desing Considerations – I. Part

In the initial stages of this study, computational design processes are conducted to establish a roadmap for integrated heat treatment and alloy design parameters, considering the following facts.

Within the scope of this study, the aim is to obtain a balance on hardness, strength, and toughness and to attain the best combination of them as much as possible. To do so, it is required to obtain graphite nodules of appropriate nodularity and quantity in a mixture of ausferrite and retained austenite[77–80]. It is known that graphite nodularity and nodule count mostly depend on chemical composition[81,82], section size, and solidification parameters[82,83]. However, neither nodularity nor nodule count can be predicted by using the Calphad methodology, for this reason, this part of the alloy design is determined through the application of prior empirical knowledge. By utilizing Calphad Approach, the only factor that can be foreseen is the volume fractions of graphite nodules. The volume fraction of graphite nodules after austenitization can be calculated using the CALPHAD approach but only if the austenitization time is long enough to reach equilibrium conditions. If not, additional diffusion simulations are required to obtain accurate predictions. However, during the analyses held, it is seen that graphite nodules reach equilibrium conditions within the specified austenitization times in every heat treatment scenario given in this study, thus, further calculations are not needed.

Austenitization temperature influences the morphology[84] and the chemical composition[85] of the austenite phase, which subsequently transforms into ausferrite. Consequently, it affects the temperature and duration of the ausferrite transformation.[24] As for austenitization time, Cheng et. al. reported that its effect on

microstructure and mechanical properties is not significant compared to austenitization temperature.[84] In the computational analyses conducted, as the austenitization temperature increases, the weight percentages of alloying elements, including carbon, in the austenite phase also increase. This leads to a decrease in the temperatures at which ausferrite transformation occurs, thereby causing a delay in the transformation. Similarly, an increase in austenitization temperature also leads to a decrease in martensite start temperature, which can be attributed to the increase in stability of retained austenite due to the relatively higher concentration of carbon and alloying elements in the austenite solid solution.[85–87] In the case of austempering treatment, generally relatively lower temperatures result in better mechanical properties[38,88]. Nonetheless, analyses indicated that if the austempering temperature is too low, the time required to complete the transformation becomes prohibitively long. In this study, when specifying austempering parameters, two critical phenomena are taken into consideration to obtain the desired ausferrite microstructures. Firstly, no pearlite or upper-bainite formation must be allowed during the cooling operation held between the austenitization and austempering processes. To achieve this, after the austenitization process, the temperature must be lowered rapidly enough to austempering temperature without intersecting the pearlite and bainite noses, whichever is more prominent. The critical cooling rate depends on the chemical composition and austenitization parameters[89,90] and it is of great importance in achieving desired mechanical properties. Fortunately, it can be determined in advance through computational metallurgy methods.[91] In this study, critical cooling rates are also taken into considerations when conducting the heat treatments. Secondly, no martensite formation must be allowed during the austempering operation. In other words, the austempering temperature must be higher than the M_s temperature of the austenite formed during the corresponding austenitization temperature. As depicted in the TTT diagrams in Figure 9, 10, 15 and 16, the specified austempering temperatures are indeed higher than the M_s temperatures, as required.

Moreover, it is considered that the retained austenite and its stability level play a crucial role in achieving the objectives of this study. It is believed that a certain

amount of retained austenite can be beneficial in terms of toughness, depending on its stability level. Hence, the aim is to acquire retained austenite that remains stable at room temperature but becomes unstable under deformation. In this way, it is aimed to leverage the martensitic transformation induced by deformation, just as in TRIP (Transformation-Induced Plasticity) steels. The TRIP effect provides materials with extra ductility and, more importantly, energy absorption capacity.[92] In this regard, it is decided to obtain samples varying volume percentages of retained austenite with different stability levels which correspond to distinct chemical compositions. All analyzes and computational design processes are conducted with careful consideration of these factors.

Firstly, the effects of essential elements for ADI, namely Carbon, Silicon, and Manganese are studied. Even when these elements are varied in the wide ranges within their standard values, their effects are found to be way weaker than expected. The final microstructures are hardly sensitive to the changes in the weight percentages of these elements. These results reveal both positive and negative implications. From the positive perspective, deviations in weight percentages of these elements that may take place during the casting processes are unlikely to affect the results significantly. On the other hand, from the negative aspect, even if considerable alterations in weight percentages are made, it is not likely to attain different results from the ones studied so far. As a result of these findings, it is decided to set the weight percentages of these elements to average values i.e., 3.4 – 3.8 wt.% for Carbon, 2.3 – 2.7 wt.% for Silicon, <0.3 wt.% for Manganese, and to focus on the effect of other elements.

The effects of Chromium, Molybdenum, and Nickel which are commonly used elements in ADI, are investigated by changing their compositions in a wide range. It is seen that increasing Chromium content results in undesired carbide formation during austempering operations. The primary purpose of Chromium is to enhance the hardenability of the ductile iron.[93] However, due to its undesirable carbide formation tendency, its decided to use it sparingly, aiming to increase hardenability without simultaneous carbide formation. Another element used to increase

hardenability is Molybdenum.[94,95] Unlike chromium, it forms carbides at higher temperatures than typical austempering temperatures (200 – 350 °C). However, high additions of it can result in formation of molybdenum carbides which are stable even at annealing conditions.[96,97] This would be detrimental to ductility and toughness properties. In addition, it retards bainitic transformation kinetics in austempering treatments more than chromium and manganese do.[98] Given that carbon diffusion is already relatively sluggish at these temperatures, this further retardation can make the heat treatment process infeasible since the time required to complete bainitic transformation becomes significantly longer. Therefore, it is decided to add only as much molybdenum as to increase hardenability, but at the same time, not to form carbides and not to prolong bainitic transformation into undesired levels. However, due to these constraints for chromium and molybdenum, their allowable amounts are found to be too low to display a considerable effect on increasing hardenability. Increasing hardenability is essential to prevent the intersection of pearlite and bainite noses during the cooling process between the austenitization and austempering processes. The addition of the elements increasing hardenability makes pearlite nose shift ahead in TTT and CCT diagrams. Moreover, these elements also affect the bainite nose in the same way and, each element affects these transformation curves in a peculiar level[99–101]. Thus, by considering these, it has been decided to add a carbide-free element into the composition, in this case, Nickel, to make a considerable increase in hardenability. Besides, it is also known that the combined effect of hardenability-increasing elements is higher compared to their individual effects.[29,40,101,102] Along with its hardenability effect, Saal et.al. reported that Nickel increases the stability of the retained austenite phase, which is present after the austempering heat treatment.[103]

Another element studied in the computational design process is Copper (Cu). Although there are studies in the literature indicating that it has positive effects on austemperability,[37,38] in the computational analyses, no considerable effect is observed in this manner. It is thought that this might be caused by a deficiency in the software database. Anyway, in view of the research in the literature reporting positive effects of copper on both austemperability and final mechanical properties,

some amount of copper is given place to the composition. However, according to the analyses held, there is a limiting factor, too much Copper addition results in some amount of liquid phase during the austempering treatment. Therefore, the quantity of copper is determined by taking these factors into consideration.

In addition, the effects of Aluminum and Cobalt are investigated. In the literature, there are studies indicating that the addition of Cobalt and Aluminum increases the bainitic transformation rate.[104,105] The analyses conducted during the computational design process showed parallel results to these findings, especially at lower austempering temperatures. Considering that transformation kinetics decrease exponentially as the temperature decreases, the presence of aluminum is significantly advantageous. It enables the practical performance of austempering treatments at lower temperatures. It is known that the bainite phase formed at lower temperatures has a finer structure and exhibits a relatively greater volume compared to the bainite phase formed at higher temperatures.[106] In addition, the presence of aluminum leads to increased carbon saturation in retained austenite, rendering it more stable against transformation into the martensite phase under mechanical and temperature-dependent influences.[54] In this regard, Aluminum has implicitly Nickel-like effects in terms of increasing the retained austenite stability. Moreover, Shayesteh et.al. reported that Aluminum promotes the graphite nucleation tendency and increases nodule count in cast iron. Nevertheless, they also note that Al addition causes a reduction in graphite nodularity.[107] Moreover, according to the analyses held, it forms some amount of liquid phase at the end of the solidification process. Yet, it is evaluated that the opportunities provided by aluminum can play an important role in reaching the purpose of this study. Accordingly, it is decided to design one of the alloys (Alloy X) containing an appropriate amount of Al in the 1st set of samples. Although Cobalt exhibits Aluminum-like positive effects in terms of accelerating bainitic transformation[104,105], it has been decided to try Aluminum first and to employ Cobalt in future studies.

As a result of all these analyses held, it is decided that the 1st set of samples, which are aimed to be used as guidance for the following set, consists of 2 different alloys (Alloy X and Alloy Y) and 2 common heat treatment processes.

5.2 Microstructure and Mechanical Property Evaluation – The 1st Set

Unfortunately, some problems were encountered in the casting process of Alloy X. When the microstructure is examined, it is seen that the graphite phase is vermicular rather than nodular (Figure 23, 25, and 26). This situation is most likely stemming from the Aluminum addition itself, and this result supports the studies[27,107,108] which focus on the effects of Al addition in ductile iron. Shayesteh-Zeraati et al. reported that Aluminum accumulation reaches the maximum value around the graphite nodules and since the pattern of this accumulation is not homogeneous and regular, this results in non-uniform diffusion of carbon.[107] Thus, this explains why graphite developed vermicular or flake-like instead of nodular in shape. However, in the literature, there are studies in which nodular cast irons are attained despite Al additions.[107,109–111]

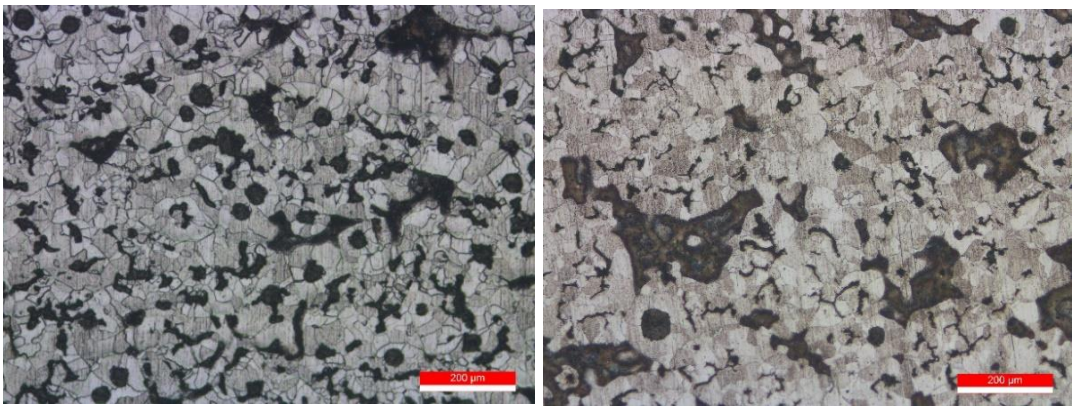

Figure 23. Alloy X – As-Cast Microstructure - Etched with 3% Nital Solution (Left - 100x, Right – 200x Magnification)

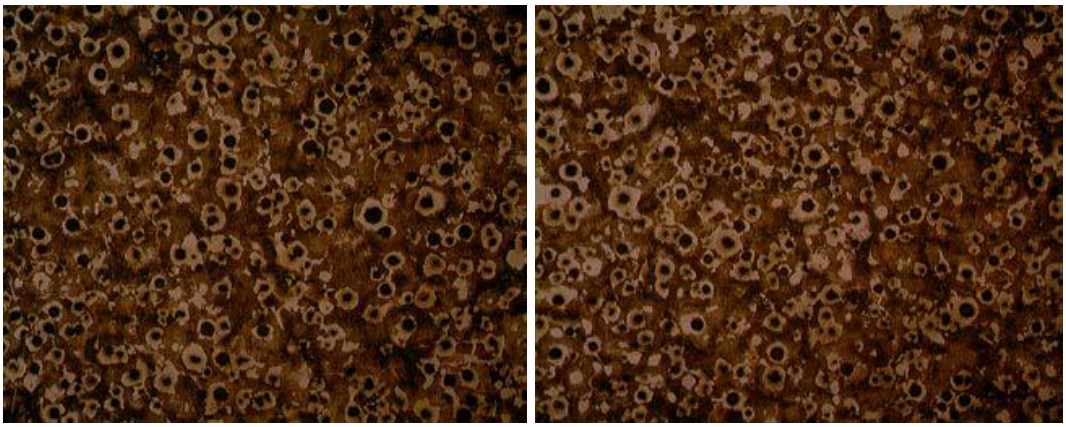

Figure 24. Alloy Y – As-Cast Microstructure - Etched with 6% Nital Solution (100x Magnification)

Table 11. Nodularity Percentages and Nodule Counts – The 1st Set

ALLOY	NODULARITY (%)	Nodule Count (Quantity/mm^2)
ALLOY X	0.2	0.6
ALLOY Y	85	150

When examining the values of nodularity and nodule count of Alloy X in Table 11, it is unfortunate to note that they are not anywhere near the expectations. Unsurprisingly, the mechanical properties are adversely affected. As seen in Table 12 and Figure 29, neither of these mechanical properties meet the requirements for this study. Nevertheless, the microstructures revealed that bainite phases are formed in the specified austempering times. This is also indicated by the fact that the retained austenite volume percentages (Table 13) are consistent with the computational calculations (Figure 30).

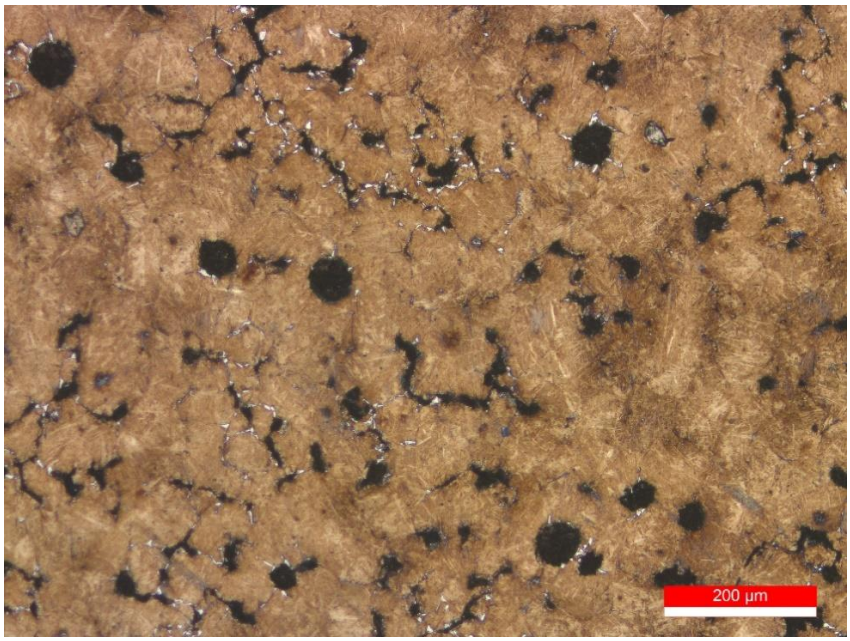

Figure 25. Alloy X - X1-250/24 Microstructure After Heat Treatment (100x Magnification)

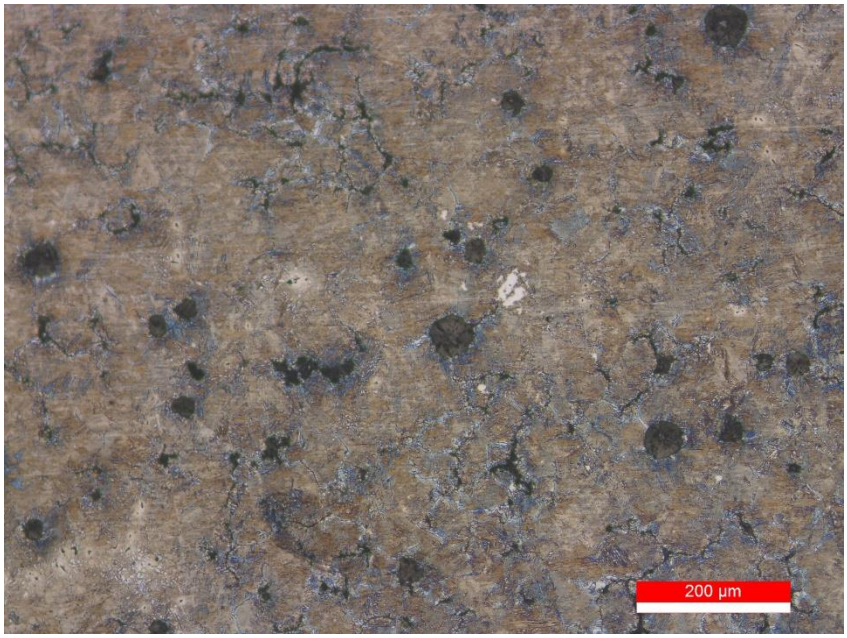

Figure 26. Alloy X - X2-350/2 Microstructure After Heat Treatment (100x Magnification)

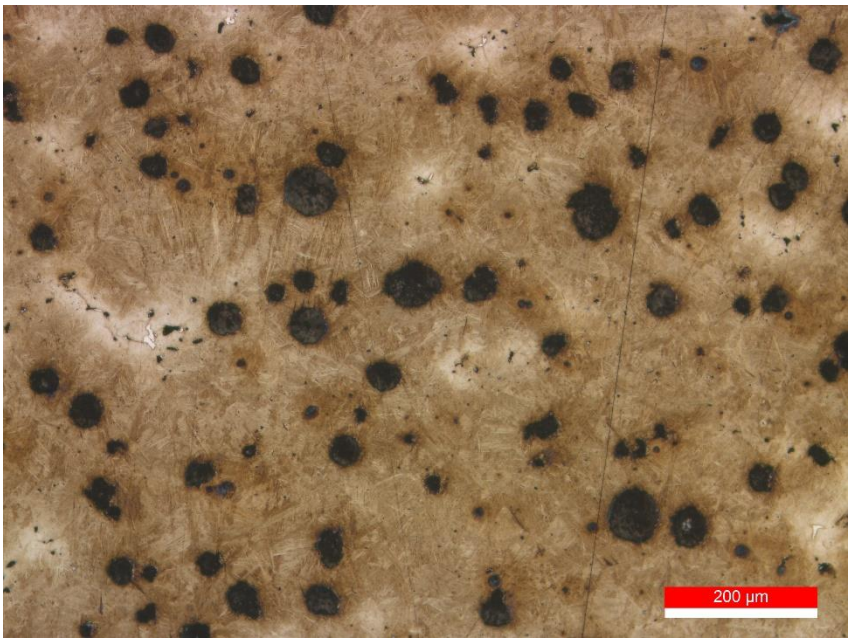

Figure 27. Alloy Y - Y1-250/24 Microstructure After Heat Treatment (100x Magnification)

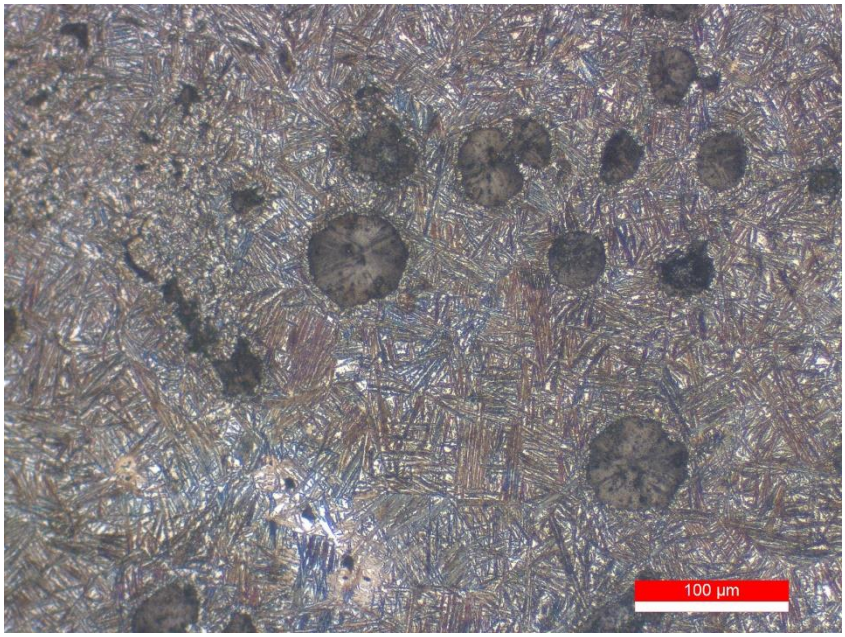

Figure 28. Alloy Y - Y2-350/2 Microstructure After Heat Treatment (100x Magnification)

On the other hand, the microstructures of Alloy Y (Figure 24, 27, and 28) show that the graphite are nodular. The graphite nodularity is measured to be 85% (Table 11). Consequently, Alloy Y samples exhibited promising mechanical properties, but some improvements were still needed to reach the target values.

Table 12. Mechanical Test Results – The 1st Set of Samples

Sample Name	Hardness (HB)	Tensile Strength (MPa)	Yield Strength (MPa)	Elongation (%)	Impact Energy (J) (25 °C)
X1-250/24	450 ± 1	675 ± 50	N/A	N/A	16.0 ± 2.3
Y1-250/24	482 ± 1	1342 ± 99	N/A	N/A	43.2 ± 4.3
X2-350/2	435 ± 6	834 ± 5	691± 28	0.8 ± 0.2	20.3 ± 5.0
Y2-350/2	424 ± 4	1031 ± 7	921± 50	4.9 ± 3.4	72.4 ± 7.6

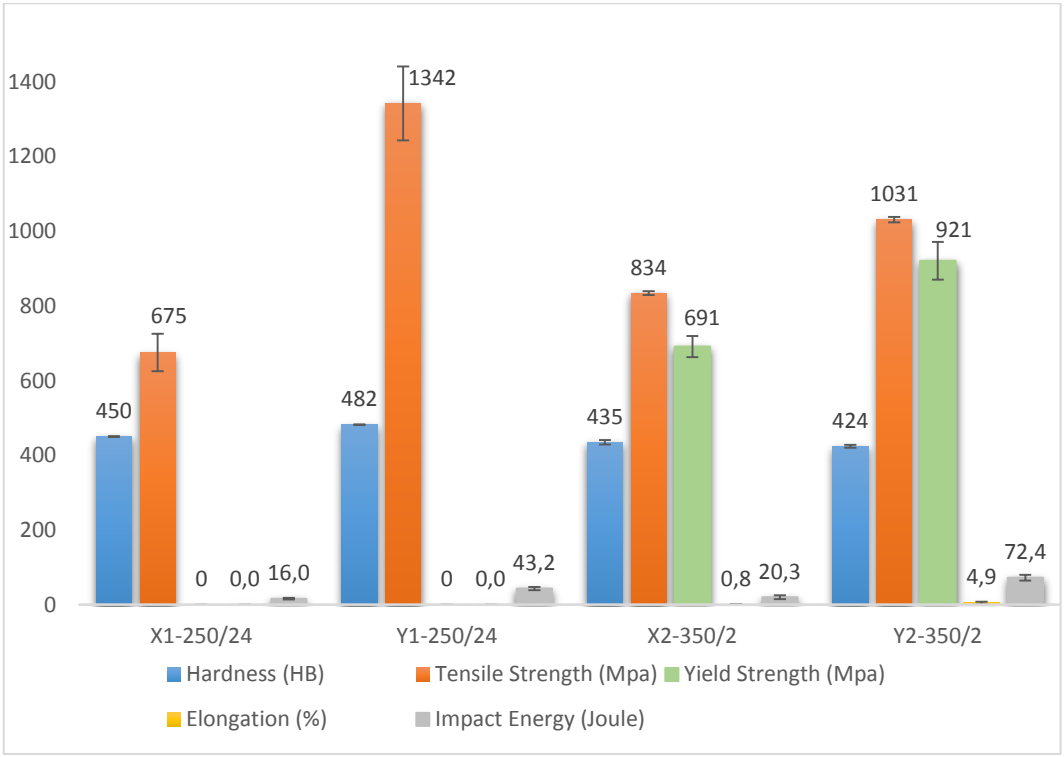

Figure 29. Mechanical Properties of the 1st Set of Samples

The mechanical test results for Y2-350/2 specimens (Table 12 and Figure 29) show satisfactory tensile strength and impact energy values. They have relatively lower hardness, but higher toughness values compared to Y1-250/24 specimens. This is expected because the Y1-250/24 specimens were austempered at a relatively lower temperature for a longer time, resulting in finer ausferrite phases in the final microstructures. The Y1-250/24 specimens have higher tensile strength and hardness due to their finer microstructures. However, they did not exhibit yielding behavior and elongation. Bhadeshia stated that when the austenite loses its percolation, in other words, becomes isolated in the microstructure, the material ends up experiencing fracture. In that study, regardless of the temperature at which bainitic transformation takes place, when austenite volume drops around 10% in volume as a result of martensitic transformation, the fracture takes place. Thus, this value is mentioned as the percolation threshold.[112] Therefore, the observation that Y1-250/24 specimens exhibited no yielding and elongation can be associated with its low volume percentage of retained austenite phase (Table 13), and certainly, also with its considerably low quenching temperature (-65 °C). By taking these into account, it can be deduced that impact energy of around 43 Joules exhibited by Y1-250/24 specimens is only related to the microstructure itself, whereas that of the Y2-350/2 specimens can be associated with the coarse microstructure because of a relatively higher austempering temperature and energy absorption due to the stress induced transformation of retained austenite.

Table 13. Retained Austenite Volume Percentages – The 1st Set of Samples (Experimental Results)

Sample Name	**Retained Austenite (vol.%)**
X1-250/24	14.7 ± 2.2
Y1-250/24	10.7 ± 1.8
X2-350/2	20.1 ± 3.8
Y2-350/2	19.5 ± 2.9

5.3 Computational Desing Considerations – II. Part

As discussed in the previous section, the 1st set experienced some unexpected problems and inadequate results that required improvements. However, this is exactly why it was decided to design two distinctive sets consecutively in the first place. Thus, the chemical compositions and the heat treatment parameters of the 2nd set of samples were determined by evaluating these results. Just as in the 1st set, it was decided that the 2nd set also consisted of 2 different alloys but at this time, each alloy had its heat treatment parameters specifically designed by considering the chemical compositions. Since the results belonging to the Alloy X specimens did not fulfil the expectations, it has been put aside at least for this study, although it is open for improvements and has many potential advantages. On the other hand, as stated above, Alloy Y specimens exhibited promising results in the 1st set. For this reason, it was decided to move on with this chemical composition. However, this time, it was aimed to obtain some ductility and to increase the retained austenite content by considering the percolation threshold. Thus, besides not specifying quenching temperatures below 0 °C in all heat treatment scenarios at this time, to increase the stability of the retained austenite through an increase in carbon and alloying elements in austenite solid solution, the austenitization temperature was increased to 920 °C.[85–87] When TTT diagrams of the Alloy Y samples in the 1st and 2nd sets (Figure 10 and 15) are compared with each other, one can see that increasing austenitization temperature results in stabilization of the austenite as expected.

Moreover, the chemical composition of the second alloy was determined with the same consideration. It was named Alloy Z, and it had almost the same chemical composition as Alloy Y but contained 2 wt.% Nickel. In this way, a higher retained austenite volume percentages were obtained as seen in Table 18 and Figure 30. To be able to make an accurate comparison as much as possible, the same austenitization temperatures and times were specified for both alloys, just as in the 1st set. Because austenitization conditions affect the incubation time and the transformation rate during the austempering treatment. Increasing austenitization temperature results in an increase in incubation time due to the increase in carbon content in the austenite

phase. The transformation rate is also adversely affected, since increasing austenitization temperature causes a decrease in nodule count i.e., a decrease in the mean distance between the nodules, hence affecting the number of ferrite nuclei formed at the beginning of the austempering process.[23–25]

Regarding the austempering parameters, a relatively lower austempering temperature was set for Z6-225/36 than for Y4-250/24 due to its higher nickel content, which results in a lower M_s temperature for the austenite phases at the austenitization temperature under equilibrium conditions. Increasing the nickel content allows for lower austempering temperatures while still being able to obtain the desired microstructure of acicular ferrite and retained austenite.[113,114] In this way, a relatively finer microstructure can be obtained.

Moreover, due to the relatively lower austempering temperature of Z6-225/36, a relatively longer austempering time was specified. However, the austempering time of 36 hours was not enough for the completion of the transformation. This duration was intentionally selected by considering the desired retained austenite volume percentage in the final microstructure. As stated in Chapter 3, during the computational design processes, the JMAK equation was employed to describe the bainitic transformation kinetics. Accordingly, this duration was also specified by utilizing the JMAK equation and as seen in Figure 30, the retained austenite volume percentage of Z6-225/36 is consistent with the one calculated by using thermocalc software. If the austempering times and the bainitic transformation completion times in Table 5 and 6, and Table 8 and 9 are compared among themselves, the austempering times are long enough to be on the safe side, except for Z6-225/36. For this reason, the other samples may not provide definitive criteria to interpret the accuracy of the JMAK equation. On the other hand, since the austempering temperature for Z6-225/36 is specified to obtain the intended retained austenite percentage, the consistency between the retained austenite percentages in Figure 30 well suggests that the JMAK equation is a convenient choice for describing the bainitic transformation kinetics in this study.

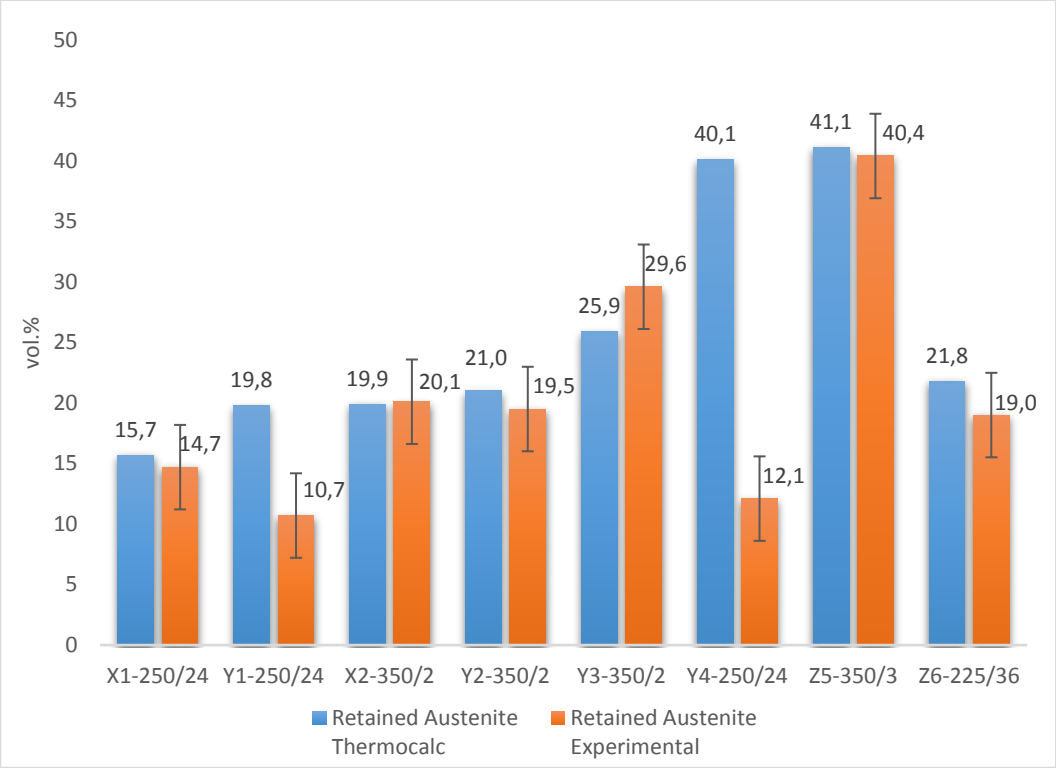

Figure 30. Comparison of Retained Austenite Volume Percentages (Thermocalc Calculations vs. Experimental Data)

However, Figure 30 reveals an inconsistency between the thermocalc calculations and the experimental results for volume percentages of the retained austenite in the Y4-250/24 specimens. The same inconsistency is also observed in the Y1-250/24 specimens. These samples have identical chemical compositions and austempering temperatures. Therefore, it is suspected that these deviations may originate from a deficiency in the software database. The Martensite Temperatures Property Model in Thermocalc software makes the relevant calculations by basing upon the models presented by Stormvinter et. al.[115] and Gulapara Hanumantharaju[116]. Stormvinter et. al. provides a semi-empirical model, whereas Gulapara Hanumantharaju has extended different models including the model offered by Stormvinter et. al.. However, since both are semi-empirical and both have stated that some improvements are still needed to enhance the accuracy of calculations for multi-component systems, these kinds of deviations are understandable.

Table 14. C_0 and Ms Values for Each Specimen After Austempering Operations (Calculated by using Thermocalc)

Specimen	Austempering Temperature (°C)	M_s (°C)	C_0 (wt.%)
X1-250/24	**250**	27	1.55
X2-350/2	**350**	82	1.26
Y1-250/24	**250**	-4	1.51
Y2-350/2	**350**	51	1.21
Y3-350/2	**350**	49	1.21
Y4-250/24	**250**	-6	1.51
Z5-350/3	**350**	59	1.10
Z6-225/36	**225**	62	1.08*

*This carbon content value given for Z6-225/36 is **not** C_0 since its bainitic transformation is not completed. This value is the carbon concentration of the retained austenite phase at the end of the austempering operation of 36 hours. (Obtained by applying the lever rule, detailed in 3.3 section.)

In Table 14, the M_s temperatures of the samples after austempering treatments and the C_0 compositions are presented. By looking at this table, one can say that the specimens austempered at relatively lower temperatures have lower M_s in the same alloy group. It is because as the austempering temperature decreases, the driving force becomes higher for more volume fraction of bainite to form, thus more carbon partitions into the surrounding retained austenite phase under equilibrium conditions. This is not valid only for Z6-225/36 since its low-temperature-austempering-treatment is ceased before reaching the equilibrium i.e., the C_0 composition is not reached in its retained austenite phase. Moreover, as seen in the same table, samples Y1-250/24 and Y4-250/24, and samples Y2-350/2 and Y3-350/2 have the same C_0 values among themselves. The reason is that they have identical chemical compositions and austempering temperatures, and the difference in austenitization temperatures does not influence C_0 value. However, as is seen, there are minor

differences among their M_s temperatures (-4 vs. -6, and 51 vs. 49, respectively). This is due to the differences in the compositions of the other elements in retained austenite phases. Austenitization temperature does not affect C_0 value, but it affects the composition of the other elements during austenitization treatment. As mentioned in Section 3.1, when making the calculations, it is assumed that the chemical composition of the retained austenite does not change during austempering operation, except for carbon.

Table 15. JMAK Constants

Sample Name	JMAK Exponent (n)	JMAK Constant (k)
X1-250/24	3.6	$2.2E^{-10}$
Y1-250/24	3.7	$5.1E^{-11}$
X2-350/2	3.1	$1.8E^{-5}$
Y2-350/2	3.4	$7.1E^{-6}$
Z6-225/36	3.5	$7.2E^{-13}$
Y4-250/24	3.4	$5.0E^{-11}$

The JMAK constant (k) and JMAK exponent (n) values are calculated for applicable samples by utilizing data obtained from the Thermocalc software. The results are presented in Table 15. The JMAK exponent value provides information about the complexity and dimensionality of the phase transformation process. As is seen, all n values are found to be within the range of $3 < n < 4$. These values suggest a three-dimensional growth mechanism. This means that the transformations are relatively slow and complex. For the JMAK constant, it quantifies the transformation rate.[117–119] Upon examination of the k values, it is observed that they are significantly influenced by temperature. The k values significantly differ for samples with the same chemical composition but different austempering temperatures, such as X1-250/24 vs. X2-350/2 and Y1-250/24 vs. Y2-350/2. Likewise, k values of Y1-250/24 and Y4-250/24 samples with identical chemical composition and austempering temperature are remarkably close. Z6-225/36 exhibits the lowest k value, which can

be associated with that it was austempered at the lowest temperature among the other samples. On the other hand, X2-350/2 has the highest k value. In addition to being austempered at a relatively higher temperature, its higher k value compared to Y2-350/2 can be attributed to the accelerating effect of aluminum on bainitic transformation.

5.4 Microstructure and Mechanical Property Evaluation – The 2nd Set

As discussed in the previous sections, the 1st set of samples experienced some unexpected problems and inadequate results that required improvements. Upon examination of the 2nd set of samples within the framework of these improvements, it is observed that the graphite were perfectly nodular in all microstructures (Figure 31, 32, 33, 34, and 35). Additionally, all the samples exhibited yielding behavior. The percentages of graphite nodularity were measured to be 95% for Alloy Y and 93% for Alloy Z (Table 16). As a result, the mechanical properties were quite good. The mechanical properties of Alloy Y samples were significantly improved compared to the ones in the 1st set. This is one of the indications that the improvements made were successful.

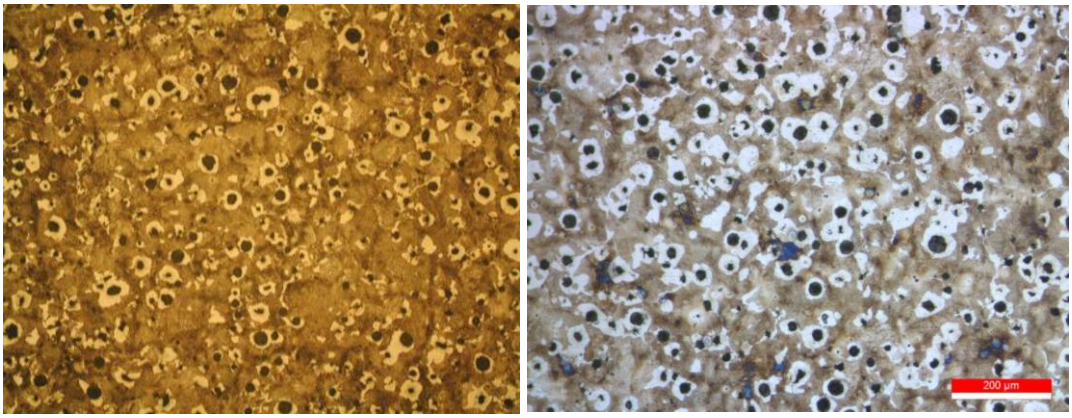

Figure 31. As-Cast Microstructures (100x) - Alloy Y, Etched with 6% Nital Solution (Left) and Alloy Z, Etched with 3% Nital Solution

Table 16. Nodularity Percentages and Nodule Counts – The 2nd Set

ALLOY	NODULARITY (%)	Nodule Count (Quantity/mm²)
ALLOY Y	95	250
ALLOY Z	93	118

Y4-250/24 has excellent mechanical properties (Table 17 and Figure 37). It has a hardness of 510 HB, and tensile strength of 1396 MPa while performing an impact energy of 44 Joules. Moreover, the size of the ausferrite phase obtained in Y4-250/24 is found to be around 200 nm (Figure 36). Normally, for a bainite phase to be called nanobainite, its size should be less than 100 nm. Yet, it is quite close to nanobainitic structure and accepted as a satisfactory achievement. As for Y3-350/2, it has relatively lower hardness and strength value, whereas relatively higher toughness value compared to Y4-250/24 since it is subjected to austempering treatment at a higher temperature. Nevertheless, it also has satisfactory results.

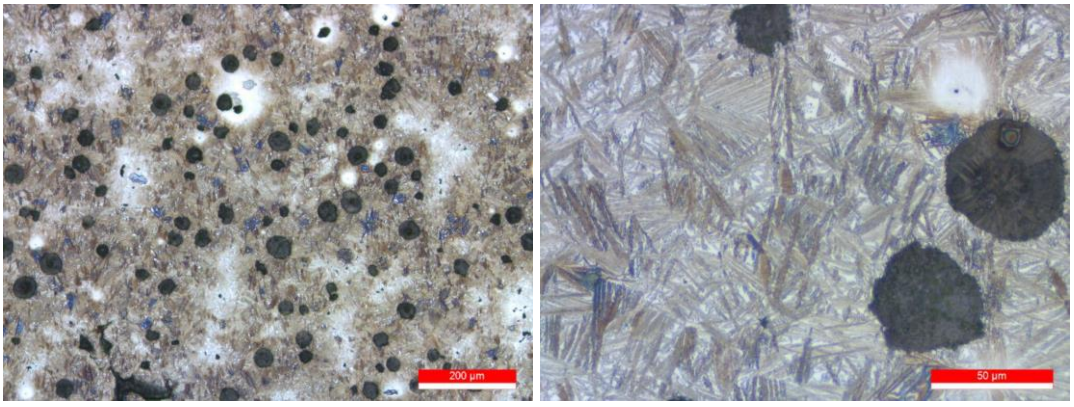

Figure 32. Alloy Y - Y3-350/2 Microstructure After Heat Treatment - 100x (Left) and 500x (Right) Magnifications

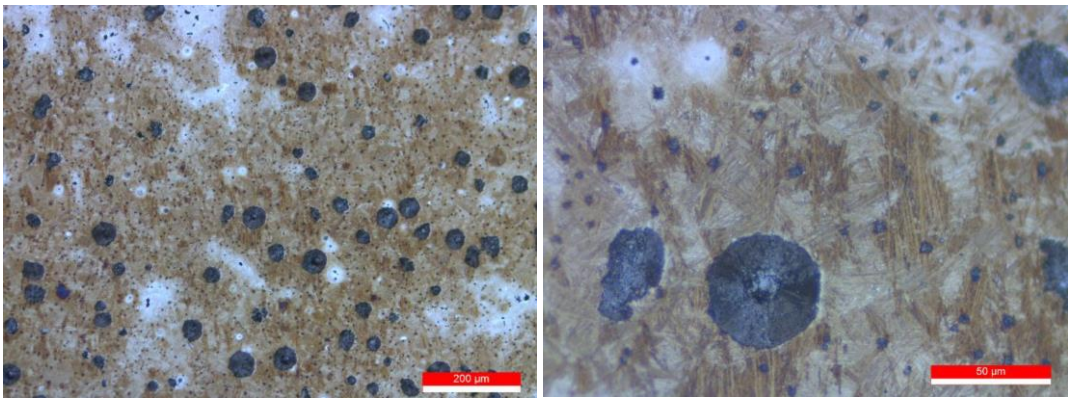

Figure 33. Alloy Y - Y4-250/24 Microstructure After Heat Treatment - 100x (Left) and 500x (Right) Magnifications

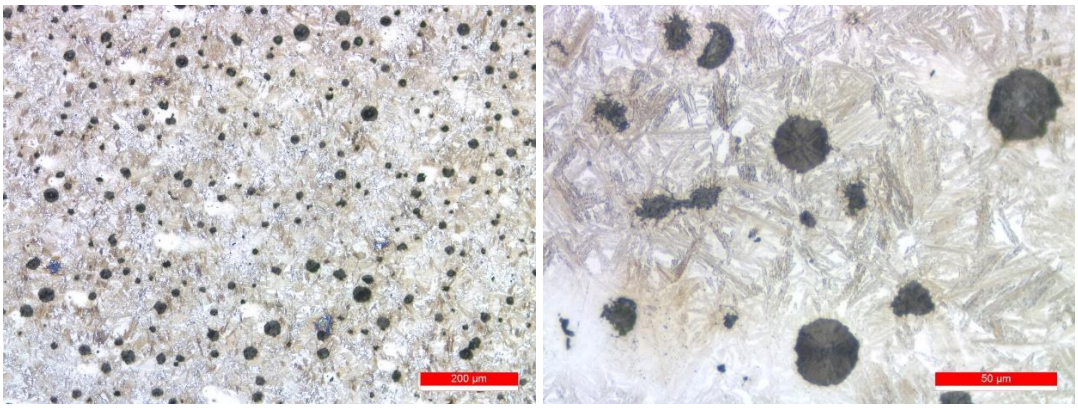

Figure 34. Alloy Z - Z5-350/3 Microstructure After Heat Treatment - 100x (Left) and 500x (Right) Magnifications

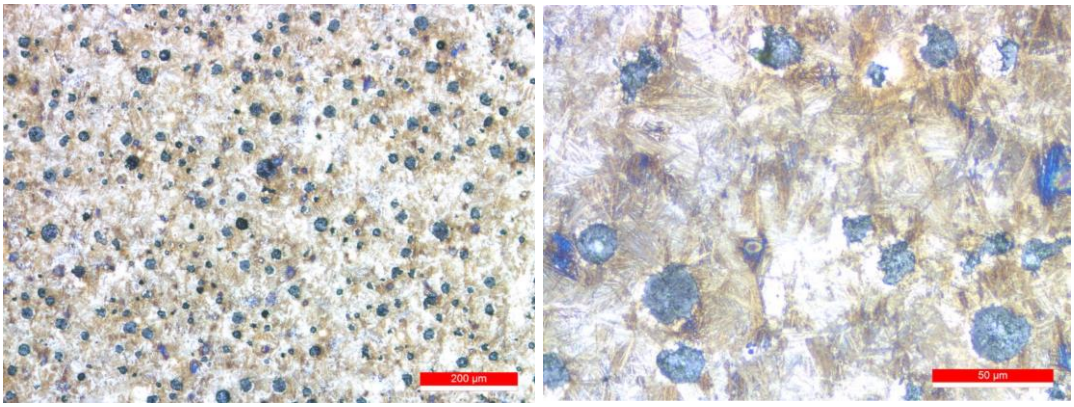

Figure 35. Alloy Z - Z6-225/36 Microstructure After Heat Treatment - 100x (Left) and 500x (Right) Magnifications

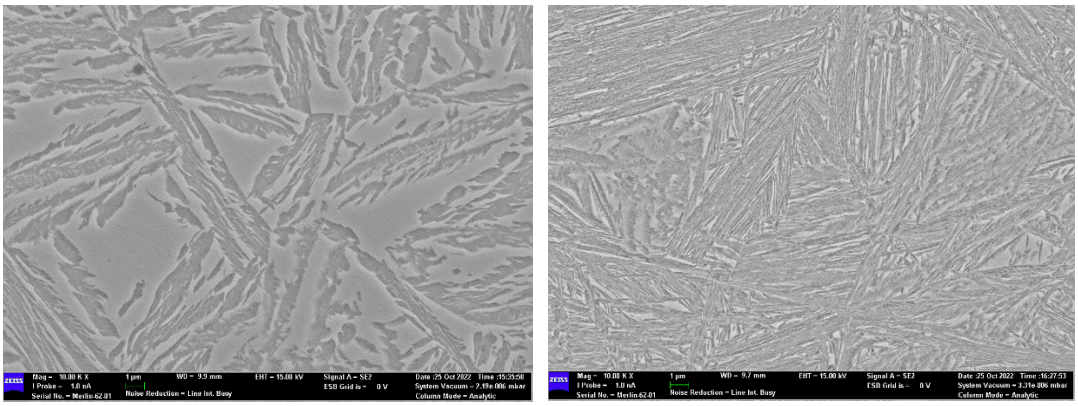

Figure 36. SEM Images of Y3-350/2 (Left) and Y4-250/24 (Right)

Z6-225/36 exhibited remarkable results in terms of the purpose of attaining an ADI with ultra-high strength and moderate toughness (Table 17). It has a hardness of 499 HB, tensile strength of 1705 MPa and yield strength of 1704 MPa while having impact energy of 41 Joules at the same time. This impact energy value is quite high for a material having these hardness and tensile strength properties. For Z5-350/3 specimens, as expected, the hardness and strength values are relatively lower than those of Z6-225/36 since they were austempered at a higher temperature. However, they are high enough to comply with the target values of ADI with high strength and high toughness. Moreover, its impact energy value is around 107 joules, and it is considerably high. This higher impact energy value indicates stress-induced martensitic transformation, and a high amount of impact energy is absorbed by this transformation. Moreover, a relatively higher elongation percentage (9%) supports this opinion. These results suggest that the approach to improving the production parameters was successful, and the computational design methodology is reliable.

Table 17. Mechanical Test Results –The 2nd Set of Samples

Sample Name	Hardness (HB)	Tensile Strength (MPa)	Yield Strength (MPa)	Elongation (%)	Impact Energy (J) (25°C)
Y3-350/2	360 ± 3	1060 ± 67	798 ± 47	2.0 ± 0.2	78.9 ± 7.8
Y4-250/24	510 ± 5	1396 ± 104	1273 ± 75	0.3 ± 0.1	44.0 ± 5.2
Z5-350/3	285 ± 1	1003 ± 42	756 ± 37	9.0 ± 1.8	107.0 ± 15.2
Z6-225/36	499 ± 7	1705 ± 3	1704 ± 5	1.8 ± 0.6	41.0 ± 8.2

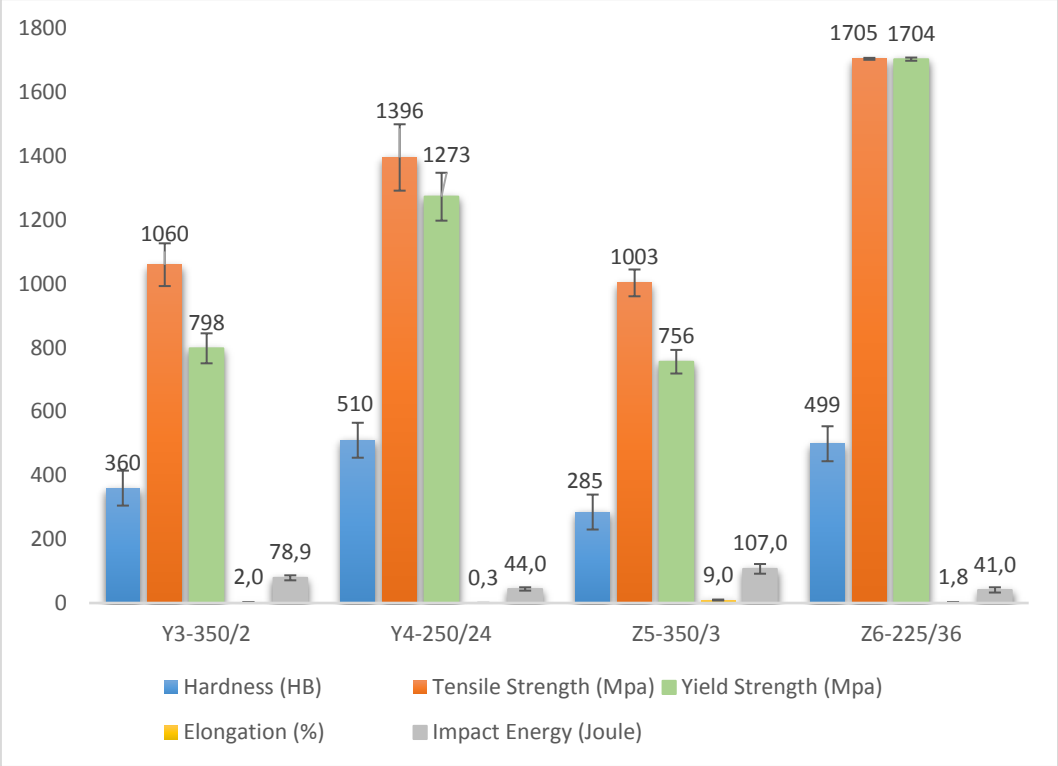

Figure 37. Mechanical Properties of the 2nd Set of Samples

Table 18. Retained Austenite Volume Percentages - The 2nd Set of Samples (Experimental Results)

Sample Name	Retained Austenite (vol.%)
Y3-350/2	29.6 ± 6.5
Y4-250/24	12.1 ± 0.8
Z5-350/3	40.4 ± 2.6
Z6-225/36	19.0 ± 3.2

When the fractography analyses are conducted for the impact test samples, it is seen that the cracks propagated along the graphite nodules (Figure 38 and 39). This indicates that graphite nodules reduce the crack propagation rate by blunting the crack tip. After each nodule absorbs some of cracks' energy, cracks proceed to propagate along them until it leads to failure. That demonstrates the importance of the graphite nodule properties in the microstructure. Alongside the effects in austenitization and austempering treatments, their shape, size, and homogeneous distribution are important for also inhibiting crack propagation.

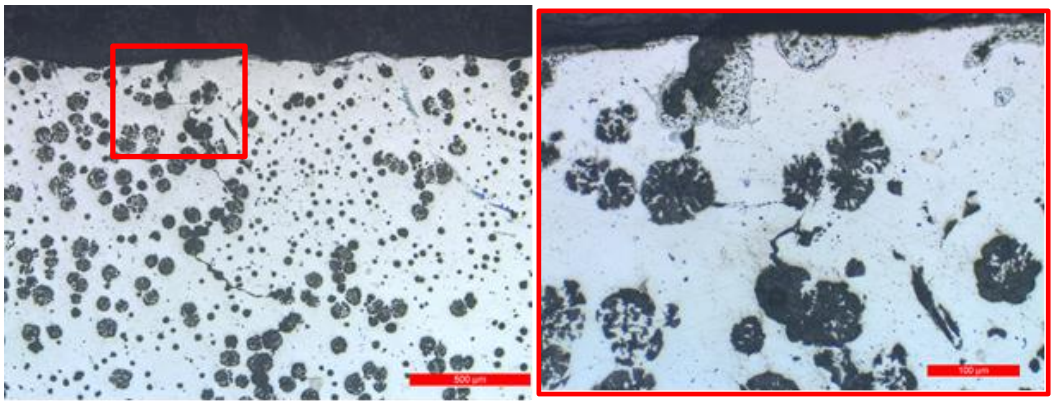

Figure 38. Y4-250/24 Sample Fractography Analysis - Crack Initiation (Left - 50x Magnification, Right - 200x Magnification)

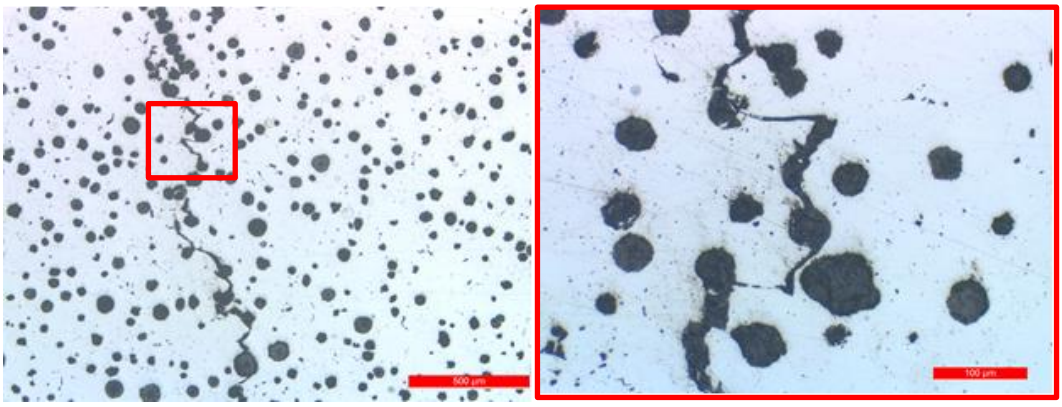

Figure 39. Y4-250/24 Sample Fractography Analysis – Crack Propagation (Left - 50x Magnification, Right - 200x Magnification)

CHAPTER 6

CONCLUSION

In this study, it has been successfully achieved the objective of designing two different Austempered Ductile Iron (ADI) materials with desired mechanical properties through the utilization of a computational design approach. Z6-225/36 specimens exhibited a tensile strength of 1705 MPa, yield strength of 1704 MPa and an impact energy of 41 Joule, whereas Z5-350/3 specimens did tensile strength of 1003 MPa, yield strength of 756 MPa and an impact energy of 107 Joules. These results comply with the study target which is attaining one ADI with ultra-high strength and moderate toughness, and another with high strength and high toughness, respectively. Furthermore, the results demonstrate that the computational design methodology used in this study provides valuable insights into designing ADI materials and has confirmed several significant findings:

- Graphite volume fraction in ADI can be estimated with a high accuracy. This finding highlights the effectiveness of computational design in predicting the microstructure of ADI after solidification and austenitization.

- Austenite composition, at austenitization temperature under equilibrium conditions, can be accurately estimated. This information is crucial for understanding phase transformation behavior during the following processes and tailoring parameters of these processes accordingly.

- Starting temperatures of pearlitic, bainitic, and martensitic transformations after austenitization can be estimated. This knowledge is important for the determination of critical cooling rate and optimizing the following austempering process, so controlling the microstructure of ADI materials. By

employing starting temperatures and calculating the other additional temperatures such as 50% bainite, 50% martensite, or 99% martensite, Time-Temperature-Transformation (TTT) curves before austempering can be accurately drawn. This information provides insights into the kinetics of phase transformations during the austempering process, which is essential for designing ADI materials with intended microstructures.

- Retained austenite volume fraction and composition after austempering process can be accurately estimated. These are essential to know for calculating final volume percentages of phases in final microstructure after quenching process. More specifically, to calculate martensite fractions based on quenching temperatures, it is critical to have knowledge of the composition of the retained austenite phase after the austempering process. The compositions are determined by calculating the C_0 values and assuming that the compositions of the rest of the alloying elements are the same as in the austenite phase after austenitization temperature. Moreover, in the case of the Z6-225/36 specimen, the results demonstrated that even if the austempering process is not conducted until the equilibrium conditions are reached, the final carbon concentration of austenite phase can be accurately calculated by using lever rule and JMAK Equation (detailed in Section 3.3).

- Final volume percentage of retained austenite can be estimated with a high accuracy. The calculations are performed employing critical martensite temperatures and regarding martensite fractions data, both of which are calculated by using the chemical composition of which retained austenite phase has after austempering. The consistency of the results in Figure 30, demonstrates the reliability of the computational design methodology in predicting the amount of untransformed austenite in ADI materials, which is crucial for understanding their mechanical behaviors.

In summary, despite the inconsistencies in two specimens (Y1-250/24 and Y4-250/24), the study's overall results emphasize the reliability and effectiveness of the computational design methodology employed within the scope of this research. It proves to be a powerful tool for designing ADI materials and estimating various critical material parameters. The findings of this research contribute to the advancement of computational design approaches in materials science and engineering and provide valuable guidance for the optimization and customization of ADI materials for specific applications.

CHAPTER 7

FUTURE WORK

In future work, emphasis will be placed on the size and distribution of the graphite phase, as it has been observed to exhibit favorable behavior in reducing the rate of crack propagation by blunting crack tips. A higher number of graphite nodules with a homogeneous distribution in the microstructure will be sought, as they can potentially serve as obstacles for crack propagation. To achieve this, the use of elements such as Al and Co will be explored as potential alternatives, as studies in literature have reported their benefits in terms of increasing nodule count. For instance, it has been reported that the addition of Co increases nodularity and nodule count, resulting in a decrease in the mean distance between the nodules.[120,121] This improvement in nodularity and nodule count may contribute to a decrease in crack propagation rate. Additionally, a higher nodule count and shorter mean distance between nodules can benefit austempering operations by accelerating the Stage I reactions and promoting more ferrite nucleation.[23,24,120,121] However, it should be noted that Co itself accelerates the Stage I reactions and widens the processing window, irrespective of its effect on nodule count.[122] On the other hand, Al has been reported to increase graphite nodules while decreasing the nodule size.[107,109,110] It also reduces the carbide formation tendency.[109,111] Thus, if the decrease in nodularity caused by Al can be overcome, it may still yield promising results. Their combined effect can also be explored since they are reported to accelerate bainitic transformation.[104,105]

In summary, in future work, the focus will be on increasing nodularity, nodule count, and homogeneous distribution of the graphite phase, while also aiming to accelerate the Stage I reactions. Based on the available literature, Al and Co are potential elements that may offer promising results in achieving these objectives. Further investigations will be conducted to explore their potential in this regard.

REFERENCES

1. ASTM A644 Standard Terminology Relating to Iron Castings. *ASTM Int.* 1–4 (2005).
2. Keough, J. R. Section IV. Austempred Ductile Iron. *Ductile Iron Society* https://www.ductile.org/didata/Section4/4intro.htm.
3. Prasad Rao, P. & Putatunda, S. K. Investigations on the fracture toughness of austempered ductile iron alloyed with chromium. *Mater. Sci. Eng. A* **346**, 254–265 (2003).
4. G, F. & H, H. Östemperlenmiş Küresel Grafitli Dökme Demirin Abrasif Aşınma Davranışı Üzerine Östemperleme Süresinin Etkisi. 16–18 (2011).
5. A. A. Nofal, El-din, H. N. & Ibrahim, M. M. Thermomechanicai treatment of austempered ductile iron. *Inst. Cast Met. Eng. - 67th World Foundry Congr. wfc06 Cast. Futur.* **2**, 798–807 (2006).
6. Bhople, N., Patil, S., Harne, M. & Dhande, S. Austempering Parameters and Machinability of Austempered Ductile Iron : A Comprehensive Review on Effective. 1197–1211 (2016) doi:10.15680/IJIRSET.2016.0502006.
7. Liu, J. Unique microstructure and excellent mechanical properties of ADI. **897**, 3 (2006).
8. ALABI, A. G. F. & ALUKO, F. I. Production And Commercialization Of Austempered Ductile Iron. *Int. J. Inov. Res. Dev.* **2**, 332–336 (2013).
9. ASTM A897/A897M-22 Standard Specification For Austempered Ductile Iron Castings. *ASTM Int.* (2022).
10. Polishetty, A. & Littlefair, G. A Comparative Assessment of Austempered Ductile Iron as a Substitute in Weight Reduction Applications. *ResearchGate* (2008) doi:10.1115/MSEC.

11. Vidyathee, G. & Singh, K. K. Thin Wall Austempered Ductile Iron: A Best Replaceable Material To Steel And Aluminum. *Int. J. Mech. Eng. Robot. Res.* **3**, 465–473 (2014).

12. Tangi, L. R. Effect of processing parameters on austempe ring behavior of alloyed / unalloyed ductile iron Effect of processing parameters on austempering behavior of alloyed / unalloyed ductile iron. (National Institute of Technology, Rourkela- 769008, 2012).

13. Keough, J. R. & Hayrynen, K. L. Automotive applications of austempered ductile iron (ADI): A critical review. *SAE Tech. Pap.* **109**, 344–354 (2000).

14. Guo, X. Correlation between austempering parameters and hardness of austempered ductile iron based on artificial neural network. **18**, 72–76 (2014).

15. Guesser, W. L., Koda, F., Martinez, J. A. B. & Da Silva, C. H. Austempered ductile iron for gears. *SAE Tech. Pap.* (2012) doi:10.4271/2012-36-0305.

16. Wang, B., Qiu, F., Barber, G. & Pan, Y. Microstructure, Wear Behavior and Surface Hardening of Austempered Ductile Iron. *ResearchGate* **9**, 9838–9855 (2020).

17. Atapek, H. Development of a boron added armor steel along the principles of physical metallurgy and evaluation of its ballistic performance. *PhD Thesis, Kocaeli Univ. Kocaeli, Turkey* (2011).

18. Crouch, I. G. *et al. Brief history: from ' Little Willie ' to ' Bushmaster '.* (2017). doi:10.1016/B978-0-08-100704-4.00002-5.

19. S. J. Cimpoeru. *The Mechanical Metallurgy of Armour Steels*. (2016).

20. Balos, S. *et al.* Geometry, mechanical and ballistic properties of ADI material perforated plates. *Mater. Des.* **83**, 66–74 (2015).

21. Balos, S. *et al.* Ballistic behaviour of austempered compacted graphite iron perforated plates. *Def. Sci. J.* **69**, 571–576 (2019).

22. Chinella, J. F., Pothier, B. & Wells, M. G. H. Processing, mechanical properties, and ballistic impact effects of austempered ductile iron. *Am. Soc. Mech. Eng. Press. Vessel. Pip. Div. PVP* **351**, 285–296 (1997).

23. Cooper, G., Roebuck, A., Bayati, H. & Elliott, R. The influence of nodule count on the austempering kinetics of a Mn-Cu ductile iron. *Int. J. Cast Met. Res.* **11**, 227–235 (1999).

24. Górny, M. *et al.* Role of Austenitization Temperature on Structure Homogeneity and Transformation Kinetics in Austempered Ductile Iron. *Met. Mater. Int.* **25**, 956–965 (2019).

25. Dakre, V., Peshwe, D. R., Pathak, S. U. & Likhite, A. Effect of austenitization temperature on microstructure and mechanical properties of low-carbon-equivalent carbidic austempered ductile iron. *Int. J. Miner. Metall. Mater.* **25**, 770–778 (2018).

26. *ASM Handbook, Properties and Selection: Iron Steels and High Performance Alloys*. vol. Volume 1 (ASM International, 1993).

27. Benam, A. S. Effect of alloying elements on austempered ductile iron (ADI) properties and its process: Review. *China Foundry* **12**, 54–70 (2015).

28. Bosnjak, B., Radulovic, B., Pop-Tonev, K. & Asanovic, V. Influence of microalloying and heat treatment on the kinetics of bainitic reaction in austempered ductile iron. *J. Mater. Eng. Perform.* **10**, 203–211 (2001).

29. Alabi, A. G. F. & Aluko, E. F. I. Production of Austempered Ductile Iron with Optimum Sulphur Level for Effective Mechanical Properties. *Int. J. Eng. Sci.* **1**, 67–71 (2013).

30. David, P., Massone, J., Boeri, R. & Sikora, J. Mechanical Properties of Thin Wall Ductile Iron-Influence of Carbon Equivalent and Graphite Distribution. vol. 44 1180–1187 (2004).

31. Gong Wenbang, Chen Guodong, Luo Li, Hao Jing, Z. Z. Design and control

of chemical compositions for high-performance austempered ductile iron. (2012) doi:1672-6421(2012)02-143-05.

32. Pravinraj, E. L., Bajwa, M. & Singh, M. Effect of varying austempering time and temperature on the mechanical properties of spheroidal cast iron. *Int. J. Innov. Res. Sci. Eng. Technol.* **3**, 12259–12266 (2014).

33. Suzuki, T., Ono, Y., Miyamoto, G. & Furuhara, T. Effects of Si and Cr on bainite microstructure of medium carbon steels. *ISIJ Int.* **50**, 1476–1482 (2010).

34. Hayrynen, K. L. The Production of Austempered Ductile Iron (ADI). *2002 World Conf. ADI* (2002).

35. Ławrynowicz, Z. & Dymski, S. Carbon concentration of austenite in austempered ductile iron (ADI). *Arch. Foundry Eng.* **Vol. 7**, **is**, 93–98 (2007).

36. Elsayed, A. H., Megahed, M. M., Sadek, A. A. & Abouelela, K. M. Fracture toughness characterization of austempered ductile iron produced using both conventional and two-step austempering processes. *Mater. Des.* **30**, 1866–1877 (2009).

37. Górny, M., Tyrała, E. & Lopez, H. Effect of Copper and Nickel on the Transformation Kinetics of Austempered Ductile Iron. *J. Mater. Eng. Perform.* **23**, 3505–3510 (2014).

38. Sahoo, S. K. A Study on the Effect of Austempering Temperature, Time and Copper Addition on the Mechanical Properties of Austempered Ductile Iron. (2012).

39. Lin, B. Y., Chen, E. T. & Lei, T. S. The Effect of Segregation on the Austemper Transformation and Toughness of Ductile Irons. *J. Mater. Eng. Perform.* **7**, 407–419 (1998).

40. Semchyshen, M. *Specialty Steels and Hard Materials*. (Pergamon Press,

1983). doi:10.1016/b978-0-08-026500-1.50001-3.

41. Yescas, M. A. & Bhadeshia, H. K. D. H. Model for the maximum fraction of retained austenite in austempered ductile cast iron. *Mater. Sci. Eng. A* **333**, 60–66 (2002).

42. Pourasiabi, H., Babazadeh, M. & Pourasiabi, H. Wear Characteristics of ADIs; A Comprehensive Review on Mechanisms and Effective Parameters. *J. Basic. Appl. Sci. Res* **3**, 646–656 (2013).

43. Darwish, N. & Elliott, R. Austempering of low manganese ductile irons. *Mater. Sci. Technol. (United Kingdom)* **9**, 572–585 (1993).

44. Bhadeshia H.K.D.H. *Bainite in Steels, Theory and Practice. Journal of Chemical Information and Modeling* vol. 53 (CRC PRESS, 2018).

45. H.K.D.H., B. & Honeycombe, R. W. K. *Steels: Microstructure and Properties*. (Elsevier Ltd, 2017).

46. Hung, F. Y., Chen, L. H. & Lui, T. S. Phase transformation of an austempered ductile iron during an erosion process. *Mater. Trans.* **45**, 2981–2986 (2004).

47. Moore, D. J., Rouns, T. N. & Rundman, K. B. The effect of heat treatment, mechanical deformation, and alloying element additions on the rate of bainite formation in austempered ductile irons. *J. Heat Treat.* **4**, 7–24 (1985).

48. Putatunda, S. K. & Gadicherla, P. K. Influence of austenitizing temperature on fracture toughness of a low manganese austempered ductile iron (ADI) with ferritic as cast structure. *Mater. Sci. Eng. A* **268**, 15–31 (1999).

49. Shanmugam, P., Prasad Rao, P., Rajendra Udupa, K. & Venkataraman, N. Effect of microstructure on the fatigue strength of an austempered ductile iron. *J. Mater. Sci.* **29**, 4933–4940 (1994).

50. Liu, J. & Elliott, R. The influence of cast structure on the austempering of

ductile iron. Part 3. the role of nodule count on the kinetics, microstructure and mechanical properties of austempered Mn alloyed ductile iron. *Int. J. Cast Met. Res.* **12**, 189–195 (1999).

51. Chiniforush, E. A., Iranipour, N. & Yazdani, S. Effect of nodule count and austempering heat treatment on segregation behavior of alloying elements in ductile cast iron. **13**, 217–222 (2016).

52. Harding, R. A. The production, properties and automotive applications of austempered ductile iron. *Kov. Mater.* **45**, 1–16 (2007).

53. Batra, U., Ray, S. & Prabhakar, S. R. Effect of Austenitization on Austempering of Copper Alloyed Ductile Iron. **12**, 597–601 (2003).

54. Aranzabal, J., Gutierrez, I., Rodriguez-Ibabe, J. M. & Urcola, J. J. Influence of the amount and morphology of retained austenlte on the mechanical properties of an austempered ductile iron. *Metall. Mater. Trans. A Phys. Metall. Mater. Sci.* **28**, 1143–1156 (1997).

55. Bhadeshia, H. K. D. H. & Edmonds, D. V. Bainite in silicon steels: New composition-property approach. *Met. Sci.* **17**, 420–425 (1983).

56. Rao, B. V. N. & Rashid, M. S. Direct observations of deformation-induced retained austenite transformation in a vanadium-containing dual-phase steel. *Mater. Charact.* **39**, 435–453 (1997).

57. Jacques, P. J., Delannay, F. & Ladrière, J. On the influence of interactions between phases on the mechanical stability of retained austenite in transformation-induced plasticity multiphase steels. *Metall. Mater. Trans. A Phys. Metall. Mater. Sci.* **32**, 2759–2768 (2001).

58. Spencer, P. J. A brief history of CALPHAD. *Calphad Comput. Coupling Phase Diagrams Thermochem.* **32**, 1–8 (2008).

59. Lukas, H. L., Fries, S. G. & Sundman, B. Computational thermodynamics: The Calphad method. *Comput. Thermodyn. Calphad Method* **9780521868**,

1–313 (2007).

60. Zhang, C. & Yang, Y. The CALPHAD approach for HEAs: Challenges and opportunities. *MRS Bull.* **47**, 158–167 (2022).

61. Thermo-Calc Software. The CALPHAD Methodology. *Thermo-Calc Software 2023* https://thermocalc.com/about-us/methodology/the-calphad-methodology/ (2023).

62. Li, X. *et al.* CALPHAD as a powerful technique for design and fabrication of thermoelectric materials. *J. Mater. Chem. A* **9**, 6634–6649 (2021).

63. Kattner, U. R. the Calphad Method and Its Role in Material and Process Development. *Tecnol. em Metal. Mater. e Mineração* **13**, 3–15 (2016).

64. *ASM Metals HandBook Volume 1 - Properties and Selections - Irons Steels and High and Performance*. *ASM International* vol. 1 (1993).

65. SSAB. Ultra-High Strength Steels (UHSS): what are they and how they improve vehicles. *SSAB.com* https://www.ssab.com/en/brands-and-products/docol/ultra-high-strength-steel.

66. Fanfoni, M. & Tomellini, M. The Johnson-Mehl-Avrami-Kolmogorov model: A brief review. *Nuovo Cim. della Soc. Ital. di Fis. D - Condens. Matter, At. Mol. Chem. Physics, Biophys.* **20**, 1171–1182 (1998).

67. Yakubtsov, I. A. & Purdy, G. R. Analyses of transformation kinetics of carbide-free bainite above and below the athermal martensite-start temperature. *Metall. Mater. Trans. A Phys. Metall. Mater. Sci.* **43**, 437–446 (2012).

68. Tian, J., Xu, G., Hu, H., Wang, X. & Zurob, H. Transformation kinetics of carbide-free bainitic steels during isothermal holding above and below MS. *J. Mater. Res. Technol.* **9**, 13594–13606 (2020).

69. ZHU, J. G. Bainite Transformation Kinetics-Microstructure Characterization of Austempered 4140 / 4150 Steel. (2019).

70. Pereira, H. B., Tschiptschin, A. P., Goldenstein, H. & Azevedo, C. R. F. Effect of the Austenitization Route on the Bainitic Reaction Kinetics and Tensile Properties of an Alloyed Austempered Ductile Iron. *Int. J. Met.* **15**, 1442–1455 (2021).

71. Chang, L. C. An analysis of retained austenite in austempered ductile iron. *Metall. Mater. Trans. A Phys. Metall. Mater. Sci.* **34**, 211–217 (2003).

72. ASTM E3-11(2017) Standard Guide for Preparation of Metallographic Specimens Standard Guide for Preparation of Metallographic Specimens. *ASTM Int.* (2017) doi:10.1520/E0003-11R17.1.

73. ASTM E2567: Standard Test Method for Determining Nodularity And Nodule Count In Ductile Iron. *ASTM Int.* **i**, 4–7 (2015).

74. *EN 1563:2018 Founding. Spheroidal Graphite Cast Irons Standard*. *European Standards* (European Standards, 2018).

75. ISO 6892-1:2019 Metallic materials - Tensile testing - Part 1: Method of test at room temperature. *Int. Stand.* (2019).

76. ASTM E975-22 Standard Practice for X-Ray Determination of Retained Austenite in Steel with Near Random Crystallographic Orientation. *ASTM Int.* **03**, 1–7 (2009).

77. Liu, C. *et al.* Effects of graphite nodule count on mechanical properties and thermal conductivity of ductile iron. *Mater. Today Commun.* **31**, 103522 (2022).

78. Wang, Z. hua, Zhang, X., Xu, F. long, Qian, K. cai & Chen, K. min. Effect of nodularity on mechanical properties and fracture of ferritic spheroidal graphite iron. *China Foundry* **16**, 386–392 (2019).

79. Al-Ghonamy, A. I., Ramadan, M., Fathy, N., Hafez, K. M. & El-Wakil, A. A. Effect of Graphite Nodularity on Mechanical Properties of Ductile Iron for Waterworks Fittings and Accessories. *Int. J. Civ. Environ. Eng.* **10**, 1–5

(2008).

80. Gundlach, R. B., Gundlach, R. B., Services, S. C. R. & Services, S. C. R. Nodularity, Its Measurement, and Its Correlation with the Mechanical Properties of Ductile Iron. *Test* (2006).

81. Dawson, S. Process Control for the Production of Compacted Graphite Iron. *Afs Cast. Congr.* (2015).

82. Liu, J. hai *et al.* Precipitation and evolution of nodular graphite during solidification process of ductile iron. *China Foundry* **17**, 260–271 (2020).

83. Riposan, I., Anca, D., Stan, I., Chisamera, M. & Stan, S. Graphite Nodularity Evaluation in High-Si Ductile Cast Irons. *Materials (Basel).* **15**, (2022).

84. Cheng, H., Fu, H., Ma, S., Lin, J. & Lei, Y. Effects of austenitizing process on microstructures and properties of carbidic austempered ductile iron. *Mater. Res. Express* **6**, (2019).

85. Bignozzi, M. C. *et al.* Effect of Heat Treatment Conditions on Retained Austenite and Corrosion Resistance of the X190CrVMo20-4-1 Stainless Steel. *Met. Mater. Int.* **26**, 1318–1328 (2020).

86. Kashefi, M. & Kahrobaee, S. Determination of martensite start temperature using an electromagnetic nondestructive technology. *J. Alloys Compd.* **720**, 478–482 (2017).

87. Kahrobaee, S. & Kashefi, M. Microstructural Characterization of Quenched AISI D2 Tool Steel Using Magnetic/Electromagnetic Nondestructive Techniques. *IEEE Trans. Magn.* **51**, 1–19 (2015).

88. Materials, P. W. Effects of Austempering Process on Mechanical Behavior Properties of Compacted Graphite Iron. (2019).

89. Dollar, M. & Gorczyca, S. Influence of Grain Size on the Work Hardening of Austenitic Stainless Steels. **1**, 177–182 (1986).

90. Babasafari, Z. *et al.* Effects of austenizing temperature, cooling rate and isothermal temperature on overall phase transformation characteristics in high carbon steel. *J. Mater. Res. Technol.* **9**, 15286–15297 (2020).

91. Erkan, A., Yılmaz, Ü. T., Cetin, B., Yalçıner, C. & Şimşir, C. Determination of the Critical Cooling Rate of Austempered Ductile Iron (ADI) Castings via Computational Metallurgy Methods. (2022).

92. Soleimani, M., Kalhor, A. & Mirzadeh, H. Transformation-induced plasticity (TRIP) in advanced steels: A review. *Mater. Sci. Eng. A* **795**, 140023 (2020).

93. Bedolla-Jacuinde, A., Hernandez-Hernandez, R. A., Guerra, F. V. & Mejia, I. The role of chromium during austempering of ductile iron. *Metall. Res. Technol.* **117**, (2020).

94. Chen, X. R., Zhai, Q. J., Dong, H., Dai, B. H. & Mohrbacher, H. Molybdenum alloying in cast iron and steel. *Adv. Manuf.* **8**, 3–14 (2020).

95. Gogolin, J. A. & Tonn, B. Impact of molybdenum on heat-treatment and microstructure of ADI. *Mater. Sci. Forum* **925 MSF**, 188–195 (2018).

96. Stawarz, M., Nuckowski, P. M. & Dojka, M. High molybdenium silicon cast iron crystallization process. *Met. 2017 - 26th Int. Conf. Metall. Mater. Conf. Proc.* **2017-Janua**, 229–234 (2017).

97. *ASM Handbook:Casting*. *Materials Park: ASM International* vol. 15 (2008).

98. Irie, T., Satoh, S., Hashiguchi, K., Takahashi, I. & Hashimoto, O. Metallurgical Factors Affecting the Formability of Cold-Rolled High Strength Steel Sheets. *Trans. Iron Steel Inst. Japan* **21**, 793–801 (1981).

99. Roger K. Steele. Considerations for the Development of Alloys Suitable for Use in In-Line Hardening of Rails, Wheels, and Tank Car Plate Having Lower Bainite Microstructures. *U.S. Dep. Transp. Fed. Railr. Adm.* (1998).

100. Mehran Maalekian. *The Effects of Alloying Elements on Steels (I).*

Technische Universität Graz (2007).

101. Totten, G. E. *Steel Heat Treatment Handbook, 2nd Edition*. (CRC PRESS, 2006).

102. ASM Handbook Committee. *ASM Handbook, Heat Treating*. vol. Volume 4D (ASM International, 1991).

103. Saal, P. *et al.* In Situ Study of the Influence of Nickel on the Phase Transformation Kinetics in Austempered Ductile Iron. *Metall. Mater. Trans. A Phys. Metall. Mater. Sci.* **47**, 661–671 (2016).

104. Caballero, F. G. & Bhadeshia, H. K. D. H. Garcia-Mateo, Caballero, Bhadeshia - 2008 - Acceleration of Low-temperature Bainite. **43**, 1821–1825 (2003).

105. Hu, F., Wu, K. M. & Zheng, H. Influence of Co and al on bainitic transformation in super bainitic steels. *Steel Res. Int.* **84**, 1060–1065 (2013).

106. Lee, S. I. *et al.* Influence of austempering temperature on microstructure and mechanical properties of high-carbon nanostructured bainitic steels. *Mater. Sci. Eng. A* **848**, 143334 (2022).

107. Shayesteh-Zeraati, A., Naser-Zoshki, H., Kiani-Rashid, A. R. & Yousef-Sani, M. R. The effect of aluminium content on morphology, size, volume fraction, and number of graphite nodules in ductile cast iron. *Proc. Inst. Mech. Eng. Part L J. Mater. Des. Appl.* **224**, 117–122 (2010).

108. GECÜ, R. Küresel grafitli dökme demirlerin aşınma davranışına alüminyum ilavesinin ve östemperleme ısıl işleminin etkilerinin incelenmesi. *Ömer Halisdemir Üniversitesi Mühendislik Bilim. Derg.* **11**, 423–430 (2022).

109. H.R. Erfanian-Naziftoosi, N. Haghdadi, and A. R. K.-R. The Effect of Isothermal Heat Treatment Time on the Microstructure and Properties of 2.11 % Al Austempered Ductile Iron. **21**, 1785–1792 (2011).

110. Kiani-rashid, A. R. & Edmonds, D. V. Microstructural characteristics of Al-

alloyed austempered ductile irons. **477**, 391–398 (2008).

111. A.R. Kiani-Rashid. The bainite transformation and the carbide precipitation of 4.88 % aluminium austempered ductile iron investigated using electron microscopy. *Elsevier* **474**, 490–498 (2008).

112. Bhadeshia, H. K. D. H. Properties of fine-grained steels generated by displacive transformation. *Mater. Sci. Eng. A* **481**–**482**, 36–39 (2008).

113. Liu, Z. *et al.* Morphology and crystallography analyses of HSLA steels with hardenability enhanced by tailored C–Ni collocation. *Metals (Basel).* **12**, (2022).

114. Huang, S. *et al.* Crystallographic insights into the role of nickel on hardenability of wear-resistant steels. *Mater. Lett.* **306**, 1–4 (2022).

115. Stormvinter, A., Borgenstam, A. & Ågren, J. Thermodynamically based prediction of the martensite start temperature for commercial steels. *Metall. Mater. Trans. A Phys. Metall. Mater. Sci.* **43**, 3870–3879 (2012).

116. Hanumantharaju, A. K. G. Thermodynamic modelling of martensite start temperature in commercial steels. 48 (2017).

117. Shirzad, K. & Viney, C. A critical review on applications of the Avrami equation beyond materials science. *J. R. Soc. Interface* **20**, (2023).

118. Starink, M. J. Kinetic equations for diffusion-controlled precipitation reactions. *J. Mater. Sci.* **32**, 4061–4070 (1997).

119. Sinha, I. & Mandal, R. K. Avrami exponent under transient and heterogeneous nucleation transformation conditions. *J. Non. Cryst. Solids* **357**, 919–925 (2011).

120. Almanza, A., Dewald, D., Licavoli, J. & Sanders, P. G. Effect of Cobalt Additions on the Microstructure and Mechanical Properties of As-cat Thin-Wall Ductile Iron. *Int. J. Met.* (2020) doi:10.1007/s40962-020-00513-3.

121. Almanza, A., Dewald, D., Licavoli, J. & Sanders, P. G. Influence of Cobalt

in the Tensile Properties of 1/2 INCH Ductile Iron Y-Blocks. *Int. J. Met.* (2020) doi:10.1007/s40962-020-00521-3.

122. Yazdani, S. *et al.* The influence of cobalt on the austempering reaction in ductile cast iron The influence of cobalt on the austempering reaction in ductile cast iron. **0461**, (2017).